



Norwegian University of
Science and Technology

Macromolecular interactions at the single-molecule level

Fluctuation analysis of bound states

Are Sæle Bruvold

Nanotechnology

Submission date: July 2018

Supervisor: Bjørn Torgers Stokke, IFY

Co-supervisor: Nina Bjørk Arnfinnsdottir, IFY
Ingrid Haga Øvreide, IFY

Norwegian University of Science and Technology
Department of Physics

Abstract

The recognition, binding and release of macromolecules are precisely orchestrated in a stochastic interplay governing all enzymatic, immunological and cellular processes. Deciphering this complex synergy in order to understand these fundamental biological processes has been a matter of active research for decades; structural models and ensemble averaging methods continue to offer insight into the vivid nature of macromolecules. Though, just as the most gifted musician cannot tell the score of a single violin through a musical ensemble, the scientist cannot tell the trajectory of a single molecule by studying molecular ensembles. Thus, in order to characterize the true fluctuating dynamics of biological macromolecules, single-molecule sensitivity is a requirement.

Here, a method for the extraction of single-molecule fluctuation parameters has been developed from the bottom up. The method combines total internal reflection fluorescent microscopy, surface immobilization, ligand-fluorescent polystyrene nanoparticle conjugation and video analysis to study the binding kinetics of macromolecular pairs. In short, videos of fluorescent nanoparticles were recorded using total internal reflection fluorescent microscopy, and their time-dependent movements were analyzed. Information on the retention times on the substrate was extracted and related to variations in the surface functionalization of both the nanoparticles and the substrate.

As a part of this, an algorithm was developed and shown to reproduce published results from the literature and extracted correct kinetic parameters from a virtually generated image series. The capability of the assay was also demonstrated by characterizing the interaction between the surface-bound polysaccharide polymannuronan and nanoparticles functionalized with its C5 epimerase AlgE4. It was found that the fluorescent polystyrene nanoparticles were inapplicable due to high degrees of unspecific binding and reliance on electrostatic stabilization. However, it is expected that utilizing more dispersible fluorescent probes with a smaller fingerprint would allow the method to be applicable for a range of macromolecular pairs at physiological conditions.

Sammendrag

Gjenkjenning, binding og utløsning av makromolekyler er presist orkestrert i et stokastisk samspill som styrer alle enzymatiske, immunologiske og cellulære prosesser. Å dechiffere disse komplekse samhandlingene for å forstå disse fundamentale biologiske prosessene har vært et aktivt forskningsfelt i tiår; strukturelle modeller og ensemble-metoder gir stadig innblikk makromolekylers levende natur. Men, på samme måte som selv den mest begavede musiker ikke kan høre notene til en enslig fiolin gjennom et musikalsk ensemble, kan ikke forskeren spore trajektoriet til et enkeltmolekyl ved å studere molekylære ensembler.

Her har en metode for ekstraksjon av enkeltmolekylers fluktuasjonsparametere blitt utviklet fra grunnen av. Metoden kombinerer total indre refleksjons-fluorescerende mikroskopi, immobilisering av biomolekyler på substrat, konjugering av ligander på fluorescerende polystyrenenanopartikler og videoanalyse. Oppsummert ble videoer av fluorescerende nanopartikler tatt opp ved hjelp av total indre refleksjons-fluorescerende mikroskopi, og deres tidsavhengige bevegelser analysert. Informasjon om retensjonstid på substratet ble ekstrahert og relatert til variasjon i overflatefunksjonalisering av både nanopartikler og substratet.

Som en del av dette ble en algoritme utviklet og vist å kunne reproducere publiserte resultater fra litteraturen, samt å hente ut riktige kinetiske parametre fra en virtuelt generert bildeserie. Metodens potensiale ble også demonstrert ved å karakterisere interaksjonen mellom polysakkaridet polymannuronan immobilisert på et substrat og nanopartikler funksjonalisert med polymannuronans C5-epimerase, AlgE4. Det ble funnet at de fluorescerende polystyren-nanopartiklene som ble brukt var uanvendelig på grunn av høy grad av spesifikk binding samt avhengighet av elektrostatisk stabilisering. Imidlertid er det forventet at ved å benytte mer løselige fluorescerende prober med et mindre fingeravtrykk, vil det være mulig å benytte metoden for en rekke makromolekyler, også ved fysiologiske betingelser.

Preface

This project was performed the spring semester of 2018 at the Norwegian University of Science and Technology (NTNU) in partial fulfillment of the requirements for the degree of Master of Science in Nanotechnology. It is a continuation of a project started the previous fall, in which most of the instrumentation, methodology for data acquisition, image analysis and processing was initiated. Some content, most notably in the theory chapter, is adapted here.

The design of the algorithm, experiments and all relevant theory was obtained or devised by the author, based on literature study and trial and failure. The experimental work was carried out at the Division of Biophysics and Medical Technology at the Department of Physics. The work will serve as a contribution to NTNU's ongoing activity on biosensors.

I would like to thank to Bjørn Torger Stokke for providing required materials, for usage of the labs and offering corrections on the report. I also thank Nina Bjørk Arnfinnsdottir for being available for questions, assistance on how to work with the chemicals, AFM instrumentation and for giving valuable feedback on the report. Furthermore, I thank engineers Astrid Bjørkøy and Gjertrud Maurstad for giving an introduction to and answering questions regarding the instruments used. Finally, I would like to express my gratitude towards family, friends and Else, without whom this work might not have come to fruition.

Contents

1	Introduction	1
2	Theory	5
2.1	Fluctuation analysis of bound states	5
2.2	The Langmuir theory of binding	6
2.3	Colloidal properties	7
2.3.1	Derjaguin-Landau-Verwey-Overbeek theory	7
2.3.2	Hydrophobic interactions	9
2.3.3	Effect of polymers	9
2.3.4	Sedimentation	10
2.4	Data acquisition methodology	11
2.4.1	Fluorescence microscopy	11
2.4.2	Atomic force microscopy	15
2.5	Video analysis and particle tracking	16
2.6	Substrate and particle functionalization	18
2.6.1	Silanization	18
2.6.2	Ligand immobilization by carbodiimide crosslinking	20
2.6.3	Mannuronan and AlgE4	21
3	Experimental	25
3.1	Materials	25
3.2	Data acquisition	26
3.3	Image analysis	27
3.3.1	Methodology	27
3.3.2	Algorithm verification and validation	28
3.4	Method development	31

3.4.1	Assessment of photobleaching	31
3.4.2	Separation of aggregates	31
3.4.3	Effect of ionic strength	32
3.5	Fluctuation analysis of AlgE4 vs mannuronan	32
3.5.1	Screening of non-specific surface adsorption	32
3.5.2	Mannuronan C5 epimerase AlgE4	34
3.5.3	Fluctuation analysis of AlgE4 vs mannuronan	34
4	Results and discussion	37
4.1	Image analysis	37
4.1.1	Algorithm verification and validation	37
4.2	Method development	42
4.2.1	Assessment of photobleaching	42
4.2.2	Separation of aggregates	44
4.2.3	Effect of ionic strength	46
4.3	Fluctuation analysis of mannuronan vs AlgE4	48
4.3.1	Screening of non-specific surface adsorption of carboxyl functionalized fluorescent nanoparticles	48
4.3.2	Mannuronan C-5 epimerase AlgE4	51
4.3.3	Fluctuation analysis of mannuronan vs AlgE4	53
4.4	Substrate functionalization characterization	56
4.5	Viability of method	58
5	Conclusion	61
A	Appendix	67
A.1	Scripts for data analysis	67
A.2	Protein sequences	76
A.3	Results from fluctuation analysis	77

Acronyms

-COOH	Carboxyl group
-NH₂	Amine group
AFM	Atomic force microscopy
APTES	(3-Aminopropyl)triethoxysilane
BSA	Bovine serum albumin
CRP	C-reactive protein
EDAC	1-Ethyl-3-(3-dimethylaminopropyl)carbodiimide
HCl	Hydrochloric acid
HEPES	4-(2-hydroxyethyl)-1-piperazineethanesulfonic acid
MeOH	Methanol
MES	4-Morpholino-ethanesulfonic acid
NP	Nanoparticle
PBS	Phosphate-buffered saline
PEG	Polyethylene glycol
RPM	Rotations per minute
SPR	Surface plasmon resonance
TIRF	Total internal reflection fluorescence microscopy
XPS	X-ray photoelectron spectroscopy

1 | Introduction

Since the first biosensor was invented by Clark and Lyons in 1962, the field has made considerable progress and the market has been expected to see astronomical growth as the technology matures [1]. It is today a main area of research at any prominent University within the natural sciences, seeking to create cheap and efficient diagnostic tools for disease biomarkers. A common working principle is to attach antibodies specific to the biomarker to be detected on a surface, inducing a signal or response upon binding [2].

The development of a sensor platform is an ongoing cross-disciplinary project at NTNU, seeking to create a portable and reusable assay for detecting the presence of specific biomarkers such as C-reactive protein (CRP). In this design, the solution to be analyzed is flowed over the sensor surface by a microfluidic device, as shown in figure 1.1. The sensor surface is functionalized with antibodies specific to the analytes or antigens to be detected, facilitating binding with a resulting change in refractive index, causing a detectable change in resonance wavelength and allowing label-free detection. This makes the optimization of the surface chemistry vital, requiring precise and efficient characterization and evaluation of the surface composition and binding kinetics [3].

The sensor project utilizes a number of characterization techniques to that end; functionalized substrates are characterized by XPS (X-ray photoelectron spectroscopy) for compositional information, AFM (atomic force microscopy) for topography and contact angle measurements for assessing the hydrophobicity. These are combined with sensitivity tests performed on the biosensor platform. The intention of this characterization is to identify parameters that are important for sensor optimization, preferably on other platforms, as the sensor production is currently expensive and time consuming.

Furthermore, all are ensemble methods, which means that the information gathered represents population averages of a large number of molecules. No single molecule is likely to behave like the average; individual molecular trajectories are obscured, meaning important information of binding kinetics is lost [4]. Thus, establishing a reproducible procedure on a cheaper, more powerful platform capable of detection at the single-molecule level is of greatest interest. This would allow efficient exploration of the surface chemistry's effect on binding kinetics in addition to regeneration and re-usability of the biosensor surface.

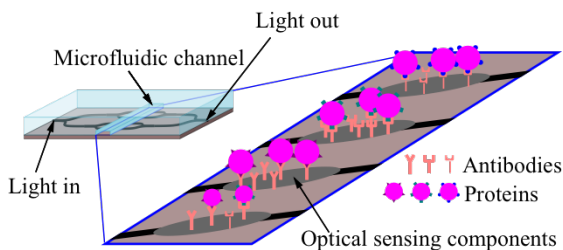


Figure 1.1: Schematic of a microfluidic biophotonic sensor, where the area of the optical sensing components are functionalized with antibodies. When antigens bind, the resulting change in refractive index is detected. Adapted with permission [5].

A novel approach towards single-molecule fluctuation analysis was reported by Gunnarsson et al. in *Nanoletters*, vol. 8, pages 183-188, 2008, utilizing total internal reflection fluorescent microscopy (TIRF) and for spatiotemporal observation of surface-bound DNA-functionalized vesicles. Fluctuation parameters were then extracted using MATLAB for video analysis [6]. The study demonstrated the capability of the assay by discriminating a single mismatch from a fully complementary DNA strand based on disparity in kinetic parameters.

Although initiated by a need to find alternative methods for characterization of a biosensor surface functionalization, this project ultimately aimed to establish a similar but more versatile single-molecule sensitive assay for the characterization of binding kinetics between a biomarker and its surface-bound ligand, expected to be transferable to numerous applications. To that end, a new procedure for the data acquisition and extraction of fluctuation parameters was established and evaluated, using a single-photon sensitive ICCD Camera equipped TIRF setup supported by an algorithm utilizing ImageJ, the MOSAIC framework and MATLAB. A goal was also to demonstrate the capability of the algorithm by surface immobilization and fluorescent nanoparticle (NP) functional-

ization of suitable macromolecular pairs, shown in figure 1.2

Chapter 2 presents the theory behind the physical principles utilized as well as the instrument and computer software used, while chapter 3 details the materials, methods and instrumentation for the data acquisition and analysis. The results and discussion are found in chapter 4. Finally, a conclusion regarding the findings along with suggestions for further work are presented in chapter 5.

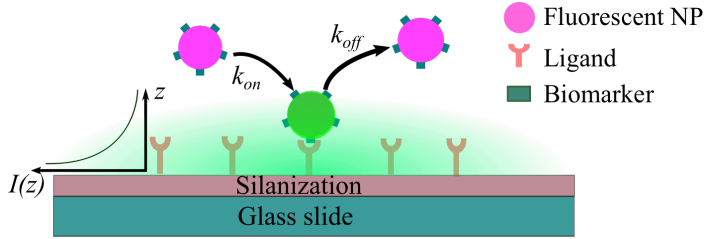


Figure 1.2: Schematic overview of the strategy used for the biomarker-ligand fluctuation analysis. Fluorescent nanoparticles are functionalized with biomarkers specific to the surface-bound ligands. Biomarkers interacting with surface-bound ligands are stationary within the TIRF field of view, and may selectively be tracked using video analysis. $I(z)$ denotes the intensity of the evanescent field set up by the TIRF. By analyzing a large number of these interactions, fluctuation parameters may be obtained. Some graphic elements used with permission [5].

2 | Theory

This section gives an overview of the underlying theory of the methods and instruments used in this project. First, the relevant theory behind the analysis of the bound states of macromolecular pairs are introduced after which the properties and forces of colloidal solutions are elucidated. Next, a primer regarding the observation of molecular probes using fluorescence and total internal reflection fluorescent microscopy is presented. An overview of surface characterization using atomic force microscopy is then given. The concepts and algorithms utilized in order to use video analysis to detect and track these molecular probes follows. Finally, the theory behind the functionalization of the sensor surface, the fluorescent sphere serving as the molecular probe and the macromolecular pairs is detailed.

2.1 Fluctuation analysis of bound states

The binding reaction between a ligand (L) and a receptor (R), forming a receptor-ligand complex, (LR), can be described by a two state model with the equilibrium constant k_d :



$$k_d = \frac{[L][R]}{[LR]} = \frac{k_{on}}{k_{off}} \quad (2.2)$$

where k_{on} is forward rate constant with units $\text{M}^{-1}\text{s}^{-1}$, while k_{off} is the reverse reaction rate constant, with units s^{-1} . k_{off} is inversely related to the residence time of the ligand,

$$t_r = \frac{1}{k_{off}}, \quad (2.3)$$

or equivalently, the mean lifetime of the protein-ligand complex.

Binding experiments are generally divided into equilibrium experiments and kinetic experiments. In equilibrium experiments, the reaction rate as a function of the concentration of one reactant is studied, giving the equilibrium constant. Kinetic experiments are more sophisticated, but yield more information. By using single-molecule sensitive assays, kinetic data such as forward and reverse rate constants can be obtained, from which the equilibrium constant also can be derived. The equilibrium constant on the other hand, reveals only the ratio between the rate constants given in equation 2.2 [7][8].

Kinetic data are often neglected parameters in biochemistry, but can be of critical importance in signal transduction. Furthermore, changes in k_{off} can result in no change in k_d , due to compensatory changes in k_{on} . This makes single molecule sensitive methods capable of retrieving rate parameters important for biosensor characterization [9].

2.2 The Langmuir theory of binding

The Langmuir theory describes the adsorption of gas molecules on a surface in relation to the pressure at equilibrium conditions. In order to model the association of biomolecules, the same theory may be applied instead considering adsorbate concentration.

From 2.2, the time-dependant forward and reverse rate equations are given by

$$\frac{\partial[LR]}{\partial t} = k_{on}[L][R] - \frac{\partial[LR]}{\partial t} = -k_{off}[LR] \quad (2.4)$$

Integrating this yields a simple exponential binding profile,

$$C_t = C_{max}(1 - \exp(-(k_{on}k + k_{off})(t - t_0))), \quad (2.5)$$

where C_{max} and C_t is the maximal or saturated and time dependent surface ligand-receptor concentration.

Only considering the dissociation phase concentration, the system may be simplified to

$$C_t = C_0 \exp(-k_{off}(t - t_0)). \quad (2.6)$$

While this is a macroscopic model, this must be reflected in individual binding events. As such, the distribution of residence times must also follow this pattern, justifying an exponential fit. [\[10\]](#)

2.3 Colloidal properties

Dissolved particles with radii of 1 to 500 nm form colloidal systems in which solution characteristics are determined by a delicate balance of van der Waals, electrostatic, solvation, born, hydrodynamic and hydrophobic interactions. At this scale $k_B T$ may be in the same order of magnitude, tipping the scale towards stability or instability, while gravitation promotes sedimentation. The presence of polymers further complicates this delicate balance, introducing additional steric and screening effects or causing bridging flocculation. As the fluorescent beads utilized in this project are in the colloidal size range, a theoretical framework for colloidal systems is required. While a complete examination is well outside the scope of this thesis, this section is an attempt at illuminating what believed to be the main driving forces of the system at hand. For a more complete account, the interested reader is referred to J. Israelachvili [\[11\]](#).

2.3.1 Derjaguin-Landau-Verwey-Overbeek theory

The Derjaguin-Landau-Verwey-Overbeek (DLVO) theory is the primary model for explaining the tendency of charged colloidal systems towards either stability or aggregation [\[12\]](#). It considers only a superposition of attractive van der Waals and repulsive screened electrostatic interactions, but has proven to be valid for surface separations down to several nanometers [\[13\]](#).

The key characteristic of electrostatic interactions between two electrolytes is the Debye length, a measure of the distance at which the electrostatic effect of a particle persists. It is defined as the distance where the electric potential is decreased by a factor of e^{-1} and given by

$$\lambda_d = \sqrt{\frac{\epsilon \epsilon_0 k_B T}{2 \rho e^2}}, \quad (2.7)$$

where ϵ and ϵ_0 are the dielectric constants of solvent and vacuum, k_B Boltzmann's constant, T the absolute temperature, ρ the number density of ionic pairs and e the elementary charge.

The electrostatic repulsive potential between two symmetric spherical colloids of radius r and charge Ze is frequently described by the Yukawa potential:

$$u_Y(R) = u_Y^0 \exp\left(-\frac{R-r}{\lambda_d}\right) \frac{r}{R}, \quad (2.8)$$

where $R = h + 2r$ is the distance between the particle centers and

$$u_Y^0 = \frac{(Ze)^2 r}{4\pi\epsilon\epsilon_0} \exp\left(\frac{r}{\lambda_d}\right) \quad (2.9)$$

The attractive van der Waal's interactions are complex, but predominantly short-ranged and may be approximated at separation distances $h \ll r$ to have an interaction energy of

$$u_w(h) \approx -\frac{Ar}{6h}, \quad (2.10)$$

where A is the Hamaker constant tabulated for various materials, typically with values $1 \cdot 10^{-20} - 20 \cdot 10^{-20}$ J. At small separation distances the energy well appears to be infinitely deep, but in reality Born or Pauli repulsion dominates at very small separations. [\[14\]](#)

Superposing the van der Waals (vdW) and electrostatic interactions gives rise to the total DLVO profile represented in figure [2.1](#) (a). At high ionic concentrations or small surface charge densities, attractive van der Waals forces dominate. At more intermediate values, an energy barrier, u_{max} , forms at separation distance h_{max} , comparable to the Debye length. The system will form a long-living metastable suspension given that the energy barrier is significantly higher than the thermal or kinetic energy of the particles. DLVO profiles for model systems with various ionic concentrations are shown in figure [2.1](#) (b). [\[15\]](#)

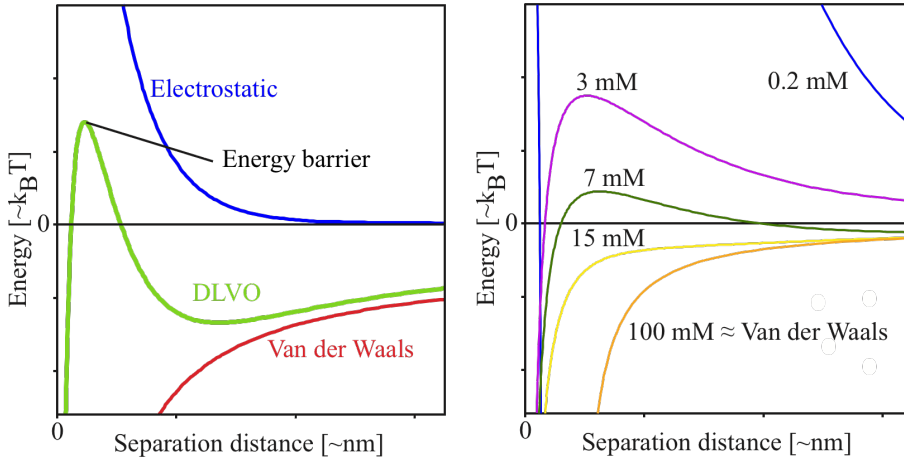


Figure 2.1: DLVO interaction energy profiles. Shown in (a) are a superposition of vdW and electrostatic forces. Displayed in (b) are DLVO interaction energy profiles at various ionic strengths.

2.3.2 Hydrophobic interactions

Hydrophobic interactions are characteristic for organic colloidal particles such as polystyrene dissolved in water. The net contribution is attractive, reducing the energy barrier and promoting aggregation. The interaction energy is given on the form

$$u_h(h) = 2\pi r\gamma\lambda_h \exp(-h/\lambda_h) \quad (2.11)$$

with the empiric parameters $\lambda_h \sim 1 - 2$ nm and $\gamma \sim 10 - 50$ mJ/m². [14]

2.3.3 Effect of polymers

Grafting polymers to colloidal particles may result in bridging attraction or steric repulsion, depending on the polymer surface density, chain length, charge, solubility and solvent characteristics. The exact nature of the interactions may not be described analytically, and no attempt will be made here. A heuristic summary is as follows: high surface densities generally promote steric stabilization, longer chains promote flocculation while polymers with charge opposite of the colloid promotes aggregation. The

solubility of the polymer governs whether it is more energetically favored with flocculation or dispersion. [16] [14]

2.3.4 Sedimentation

The competition of gravity promoting sedimentation and entropy tending towards mixing results in an equilibrium sedimentation profile obeying Boltzmann statistics described by

$$\frac{\partial P(\rho(z))}{\partial z} = -mg\rho(z), \quad (2.12)$$

where $P(\rho)$ is the osmotic pressure, ρ the colloid number density, z the height, m the particle mass and g the gravitational acceleration. In the ideal, dilute system, inter-colloidal interactions may be ignored and the equilibrium sedimentation profile is barometric and the volume fraction is given by

$$\mu(z) = \mu_0 \exp\left(\frac{-z}{L_g}\right), \quad (2.13)$$

where μ_0 is the volume fraction at $z = 0$ and L_g is the gravitational length,

$$L_g = \frac{k_B T}{\frac{4}{3}\pi r^3 \Delta\rho g}, \quad (2.14)$$

with r the colloid radius and $\Delta\rho$ the colloid-solvent density mismatch [17]. Thus, for polystyrene NPs with radii of $100 \cdot 10^{-9}$ m, $\Delta\rho$ of 0.05 kg/m^3 , at T equals 296 K and 9.81 m/s^2 for g , a L_g of 2 mm is obtained. The eppendorf tubes used for the particle solutions in the present study have a diameter of 11 mm and length of 40 mm , while the droplets applied to the substrate have heights of approximately 1 mm . This implies that a sedimentation profile will form over time [18].

The kinetics of the system need to be considered in order to find the time expected for the system to reach the sedimentation profile described. A valid approach is ignoring non-Newtonian forces, using Stokes' Law [19]. The sedimentation velocity is then given by

$$v_s = \frac{2g\Delta\rho r^2}{9\eta} \quad (2.15)$$

It is useful to note that L_g corresponds to the ratio $\frac{D}{v_s}$. Inserting for η , the dynamic viscosity of water, we get a sedimentation velocity of 270 nm/s [20]. Considering the

experimental dimensions specified, the theory outlined suggests time scales for sedimentation in the eppendorf tube and on the coverslide to be tens of hours and one hour, respectively. Thus, in order to keep particle concentrations constant across experiments, mixing is required.

Assessing whether gravitational driven irreversible sedimentation may be neglected by ensuring that the gravitational length is much greater than the particle diameter,

$$Pe = 2r/L_g \ll 0.1. \quad (2.16)$$

This is referred to as the Peclet number and establishes the ratio of gravitational potential energy to thermal energy [21]. Another more heuristic approach is calculating the characteristic transport lengths over a specified time interval [22] [23]. For a complete account on the current state of research in particle settling, the reader is referred to the excellent review by Piazza [24].

2.4 Data acquisition methodology

2.4.1 Fluorescence microscopy

Fluorescence is the emission of a photon due to relaxation of an excited orbital electron. When a photon with the energy $h\nu_{ex}$ interacts with an orbital electron of a fluorescent atom molecule, it is excited from state S_0 to a higher energy state S_1 ,

$$S_0 + h\nu_{ex} \rightarrow S_1. \quad (2.17)$$

A subsequent relaxation process releases the energy through the emission of another photon, $h\nu_{em}$, a few nanoseconds later, while some energy is dissipated as heat,

$$S_1 \rightarrow S_0 + h\nu_{em} + \text{heat}. \quad (2.18)$$

Thus, the emitted photon has lower energy with a corresponding longer wavelength, as can be seen in figure [2.2]. This energy change, referred to as the Stokes' shift, is utilized in fluorescence microscopy by separating emitted photons from absorbed excitation photons with appropriate optical filters.

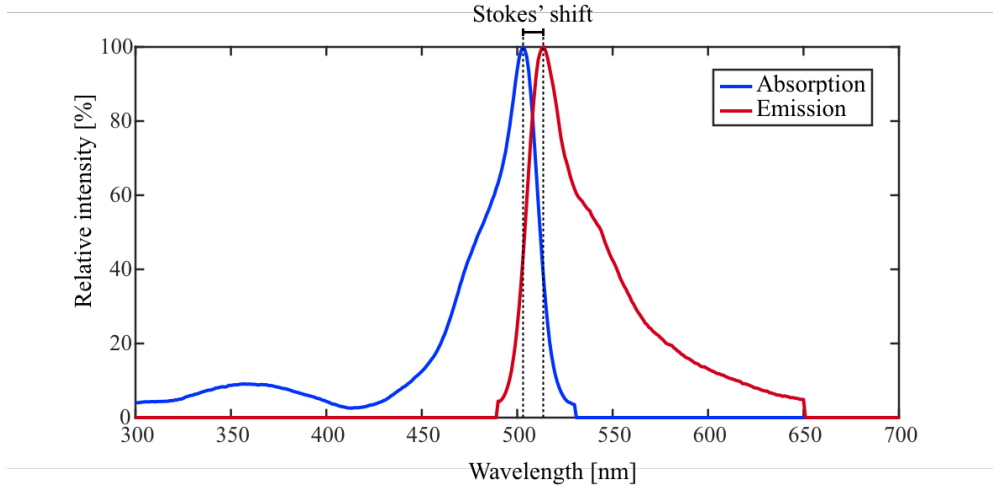


Figure 2.2: The absorption and emission spectra of yellow-green fluorescent NPs F8764 from Thermo Fisher, exhibiting a Stokes' shift of approximately 11nm [25].

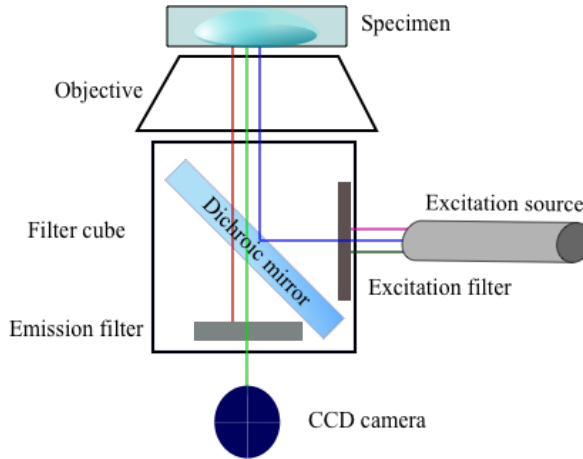


Figure 2.3: Basic schematic of a fluorescent microscope. The blue line represents light traveling from the source through an excitation filter and being reflected by a dichroic mirror onto the specimen. Light from the specimen travels back through the filter cube and the dichroic mirror. Before reaching the CCD camera or ocular, the emission filter removes unwanted light, shown in red. Finally, only the emission photons represented by the green line are passed to the ocular or CCD camera.

Fluorescent molecules typically have a broad spectrum of absorption or excitation and emission wavelengths that frequently overlap, necessitating correct choice of filters. A typical schematic of the apparatus is shown in figure 2.3. Generally, a filter cube with an excitation filter, a dichroic mirror and an emission filter is used. The excitation filter serves to make the wavelength distribution narrower before hitting the sample, while the emission filter removes excitation photons by only passing on photons emitted from the sample by fluorescence. The dichroic mirror selectively reflects shorter wavelength excitation photons back on to the sample, while longer wavelength emission photons are transmitted [26]. A weakness of traditional fluorescence microscopy is that fluorophores outside the focal plane are excited, causing background noise to be an issue. Several strategies have been developed to alleviate the problem of background fluorescence, one of which is using total internal reflection to selectively excite fluorophores close to the sample-objective interface.

Total internal reflection fluorescence microscopy

Total internal reflection fluorescence microscopy (TIRF) utilizes total internal reflection to selectively excite particles plane close to the interface from which the laser originates, significantly increasing resolution and signal-to-noise ratio. As noise is detrimental for video analysis and tracking, TIRF is an absolute necessity for the methodology developed. As biosensor receptors or antibodies are surface-bound, TIRF is an ideal technique for observing the kinetics of macromolecules in the proximity of the surface. Total internal reflection can be explained by geometrical optics.

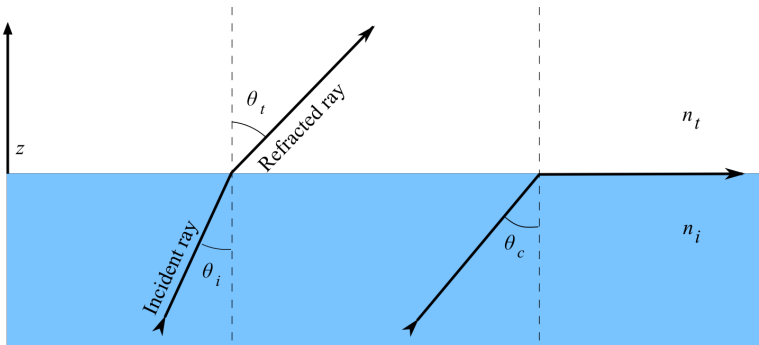


Figure 2.4: Refraction of light travelling through two transparent media with different refractive indices, $n_i > n_t$. To the right, total internal reflection is observed due to the angle of incidence being at the critical angle, θ_c

When light travels across the interface between two transparent materials with different refractive index as shown in figure 2.4 it will refract according to Snell's Law,

$$n_i \sin \theta_i = n_t \sin \theta_t, \quad (2.19)$$

where light travels through medium i with refractive index n_i to medium t with refractive index n_t . In the case of light travelling from a medium of higher to a medium of lower index, the light is refracted at an angle greater than of the incident beam. At a certain incident angle, θ_i , the refracted ray will be parallel to the surface. This is referred to as the critical angle, θ_c , and follows directly from Snell's Law by inserting 90° for θ_t :

$$\theta_c = \arcsin \left(\frac{n_t}{n_i} \right). \quad (2.20)$$

For incident angles larger than this critical angle, the light will be reflected and some incident energy propagates along the surface, creating a standing wave and an evanescent field localized at the interface, with intensity decaying exponentially with distance z from the surface.

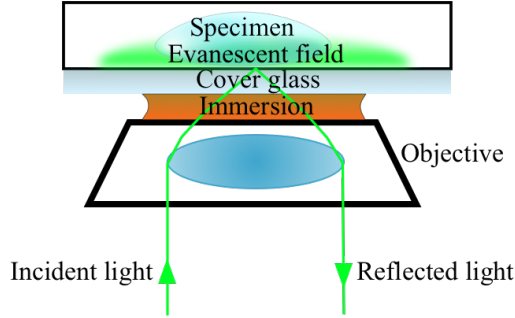


Figure 2.5: Showing the objective and stage of a TIRF setup, the incident light at an angle such that an evanescent field is formed across the specimen surface.

The intensity of the evanescent field at distance z above surface is given by

$$I(z) = I_0 e^{-z/d}, \quad (2.21)$$

where I_0 is the intensity at $z = 0$ [26]. The depth of the evanescent field, defined as the distance at which the excitation decays to $1/e$, is given by

$$d = (\lambda_0/4\pi)(n_i^2 \sin^2 \theta_i - n_t^2)^{-1/2}, \quad (2.22)$$

where λ_0 is the vacuum wavelength of the light. d generally ranges from 70 to 150 nm, and is dependent on the wavelength of the incident light. Refractive indices are set by the experiment. Generally $n_i = 1.518$ for the glass slide and immersion oil, while $n_t \approx 1.330$ for the sample, in this case water. For biological samples, it may be unknown or variable, necessitating angle of incidence to be well above estimated critical angle.

Photobleaching

Photobleaching is the degradation of a fluorophore's ability to fluoresce due to gradual photon-induced degradation. Fluorophores may interact with other molecules upon transition, causing permanent irreversible modifications of the fluorophore and thus its electronic properties. The rate at which photobleaching occurs greatly varies between fluorophores. For experiments extending over time, it is essential to use fluorophores which exhibit a low rate of photobleaching. For TIRF, bound fluorophores with prolonged exposure to the high intensity evanescent field will be more susceptible to bleaching than particles freely diffusing in and out of the evanescent field. To avoid experimental results being influenced by this effect, it is possible to detect and filter photobleached particles in the data analysis. [27][28]

2.4.2 Atomic force microscopy

Atomic force microscopy (AFM) utilizes an atomically sharp solid probe attached to a flexible cantilever, raster scanning across the sample in order to retrieve surface topography. The cantilever has a known spring constant, allowing measurement of the force between sample and tip as a function of vertical displacement. A piezoelectric positioner controls movement vertically and horizontally by applying a voltage across the piezoelectric tube wall, contracting or expanding the tube. A basic AFM schematic is shown in figure [2.6]

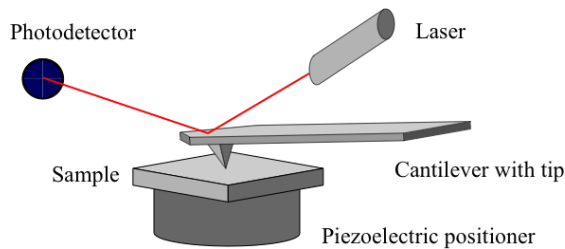


Figure 2.6: Simplified schematic of an AFM setup. The laser is deflected at the base of the tip, allowing the photodetector to precisely map vertical and horizontal displacement. Tip position is controlled by the piezoelectric positioner.

AFM utilizes the surface contact forces between the tip and the sample to acquire surface topography for solid materials. There are several different modes of operation with varying complexity. In the most basic mode, contact mode, the tip and surface is kept so close that the interaction force between the tip and sample is repulsive. Either the tip will follow the surface by adjusting the height with the piezoelectric positioner in order to keep the force constant (constant deflection), or the tip will be held at constant height (variable deflection), the topography calculated based on the deflection forces on the cantilever. Note that the cantilever will also bend due to the repulsive forces, keeping it from crashing into the sample. However, very sharp features and uneven surfaces ($> 10 \mu\text{m}$) will cause the tip to crash. The servo system may also be disabled, using the AFM to pattern the surface.[29](#) [30](#)

2.5 Video analysis and particle tracking

The first step in the video analysis of biological image data, is the detection and tracking of objects of interest. Here, objects are functionalized fluorescent NPs and appear in the image as bright spots, where each spot occupies only a few pixels. Each pixel in the image is recorded and mapped to a bit depth of 8, each pixel being assigned a value of 0 to 255 depending on the intensity of light at the corresponding position. From this, the particles can be tracked spatially and temporally. A wide range of possibilities exist to this end, ranging from manual tracking by hand to sophisticated programming using artificial intelligence [31](#) [32](#). Part of this project was finding and evaluating an efficient procedure for the image analysis in order to extract fluctuation parameters from a large amount of particles. This analysis forms the basis for this project. Many

softwares were explored, IDL, ICY and several java solutions, eventually settling on MOSAIC's plugin suite for ImageJ. This being due to the software being compatible across several platforms, open-source and under continuous development. Furthermore, an efficient GUI allows visual inspection of the successfullness of the detection. It has also proven to score well in objective comparison with other particle tracking solutions [33]. Note that the primary purpose of MOSAIC is detecting spatial trajectories of moving particles, and as such the usage for determining fluctuation parameters is a novel application.

The algorithm underlying MOSAIC's particle tracker start by determining minimum and maximum intensity across all frames of a movie or sequence of images, normalizing to values between 0 and 1. Noise due to non-uniform sensitivity in camera pixels or uneven illumination and discretization noise from the digital camera is corrected for using a boxcar average and a Gaussian normalization over a square region larger than user-set radius of objects to be detected. The positions of objects to be tracked are then determined by identifying local intensity maxima. If a maxima is in the upper, user-set percentile or threshold value of the intensity values of a frame and no brighter pixel is within a pixel distance of the user defined parameter, r , it is recognized as a candidate object. Note that as the intensity percentile is calculated on a frame per frame basis in order to make the algorithm robust against change in intensity over time due to bleaching or drift of focus over time. Unfortunately, this implementation is counteractive for analysis where the amount of particles in the field of view may change and thus also the intensity, and posed a challenge for this project. However, the latest version available from github allowed the absolute intensity value to be used as a threshold. Once recognized as an object of interest, the centroid position is refined to account for noise. A further refinement is required in order to filter false detections and aggregates. A non-particle discrimination algorithm is applied, utilizing that aggregates have different intensity distributions in order to filter them out. A particle discrimination score is given, where higher score indicates greater likelihood of the object being real. Any objects with a score lower than an user-set threshold value are discarded by the program.

For temporal analysis, positions across multiple frames are compared in order to identify a physical particle across multiple frames. An user-set displacement predefines the maximum displacement per frame, while link range determines the amount of subsequent frames analyzed in order to determine the trajectory. More options exist, but are irrelevant for the purpose of fluctuation analysis of bound states [31].

The relevant output parameters of MOSAIC are: intensity, position and non-particle discrimination scores. These are grouped into trajectories, giving spatiotemporal information of bright objects, in this case fluorescent spheres, recognized over multiple frames.

2.6 Substrate and particle functionalization

Part of the motivation for the procedure developed for fluctuation analysis, was an alternative characterization method for the surface functionalization of a biosensor. As such, the biosensor surface functionalization strategy, silanization and subsequent immobilization of antibodies, was adapted to this platform. In addition, in order to expand the applicability, the molecular pair AlgE4 and mannuronan was investigated. Here is presented an introduction to the surface chemistry and macromolecular pairs used for immobilization.

2.6.1 Silanization

The sensor surface needs to be functionalized to minimize unspecific binding and to allow the capture antibodies to be permanently bound in a controlled manner. As the change in refractive index is entirely dependent on surface composition and topography, precise control and reproducibility of the surface chemistry is required for optimal sensor performance. For practical and commercial purposes, robustness in physiological conditions, low cost and the ability to mass produce are also of interest [34]. A range of possibilities exist to this end, but for silica based substrates, the most relevant procedures utilize self-assembly in either phosphonate-, organosilane- or glutaraldehyde-based procedures. An organosilane-based approach using amine as a crosslinker has previously been used by the group, and has been found to produce layers exhibiting relatively high physical and chemical stability [35]. While the process has been thoroughly scrutinized, there is no consensus regarding the reaction mechanism and the process is largely dependent on reaction conditions [34].

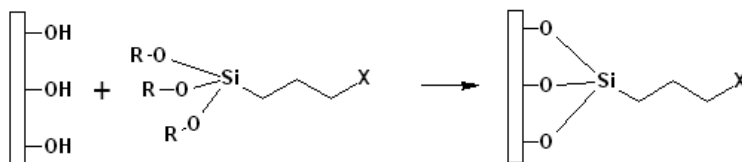


Figure 2.7: A schematic illustration of the overall reaction of an organosilane with the functional group X binding to exposed hydroxyl groups at the glass surface, forming a covalent bond.

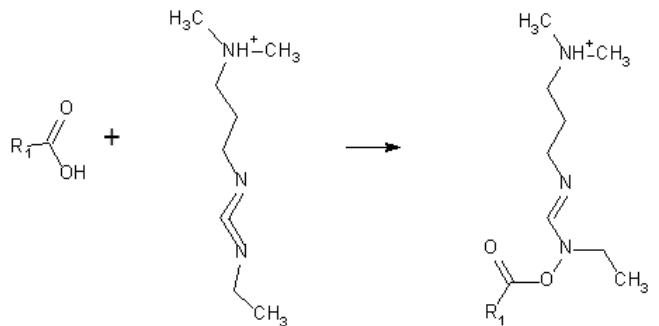
Organosilane procedures, often referred to as silanization, utilizes the reactivity between exposed hydroxyl groups of silanols at glass surfaces and the siloxanes in the organosilane, causing a condensation reaction between the two, leaving the functional group of siloxane, denoted X in figure 2.7, as a functional group on the surface that may be conjugated to a protein or antibody of interest. For our experiments, amine was the functional group of choice.

To ensure a high density of silanol groups at the glass surface and to remove organic contaminants, the first step of silanization is a cleaning or activation procedure. A range of procedures exist, where plasma cleaning and immersion in piranha solution are recurrent. The biosensor group at NTNU has found a 1:1 volume percent solution of concentrated HCL and methanol to be efficient. Silanization should be performed in succession with cleaning in order to avoid degradation of the silanol or introduction of contaminants. A range of organosilanes is applicable, though APTES (3-aminopropyltriethoxysilane) has been most extensively used due to high reactivity and low carbon count, creating uniform and relatively thin layers, practical for surface-sensitive applications as here 36.

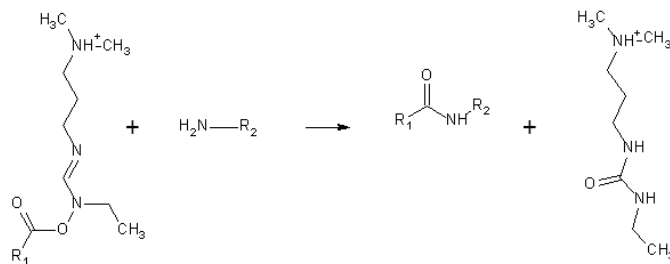
Note that both head and tail groups may bind to the hydroxyl groups at the surface, and that cross-linking of alkoxy silane may cause multiple layers to be deposited, depending on APTES concentration and reaction time. Thus, control of reaction time by the removal of APTES solution is required to stop oligomerization.

2.6.2 Ligand immobilization by carbodiimide crosslinking

Once the surface is aminated through silanization, antibodies may be immobilized on the surface by covalent attachment or by adsorption. For longevity, covalent attachment is preferred. EDAC (1-Ethyl-3-(3-dimethylaminopropyl)carbodiimide) is a crosslinker, allowing terminal amine groups to undergo a condensation reaction with carboxylic acids, similar to how peptide bonds are formed. EDAC forms a reactive intermediate with carboxylic acids, O-acylisourea, which is substituted by a primary amino acid on the protein or antibody to be immobilized. Thus, an amide bond is formed while isourea is released into the solution.



(a)



(b)

Figure 2.8: Shown in (a) is the reaction between a carboxylic acid and EDAC, forming the intermediate product o-Acylisourea. The functional group, R_1 , here denotes a protein. In (b), o-Acylisourea further reacts with a terminal primary amine. The end product is an amide bond between the carboxylic acid containing compound and the molecule with the primary amine. Isourea is released as a by-product.

EDAC crosslinking is most efficient in acidic conditions and must be performed in buffers devoid of extraneous carboxyls and amines. MES (4-morpholinoethanesulfonic acid) is a particularly suitable carbodiimide reaction buffer. Phosphate buffers and neutral pH conditions are compatible with the reaction chemistry, albeit with lower efficiency; increasing the amount of EDAC in a reaction solution can compensate for the reduced efficiency. Note that the intermediate is unstable in water, and will be hydrolysed while the carboxylic acids regenerate [37] [38] [39]. The fluorescent spheres serving as the molecular probes generally come with prefunctionalized groups, allowing carbodiimide crosslinking chemistry to be used for the covalent attachment. While the chemistry is identical, working with a colloidal solution poses additional challenges. This is related to cleaning and separation as well as interactions between multiple spheres [40].

2.6.3 Mannuronan and AlgE4

Alginates are linear homo- or copolymers consisting of monomers $(1 \rightarrow 4) - \beta$ -D-mannuronic acid (M) and $(1 \rightarrow 4) - \alpha$ -L-guluronic acid (G) joined by glycosidic linkages. Unlike most polysaccharides, monomer variations are introduced not during polymerization but in a consecutive epimerisation by various C-5 epimerases in the AlgE1-7 family. This accounts for the large sequential and compositional variations observed, with M-blocks, G-blocks or alternating M- and G-monomers [41].

Mannuronan is an alginate and a homopolymer of $(1 \rightarrow 4) - \beta$ -D-mannuronic acid, serving as the precursor from which other alginates are synthesized by epimerization. The exposed carboxyl groups allows attachment to terminal amine groups by carbodiimide crosslinking chemistry.

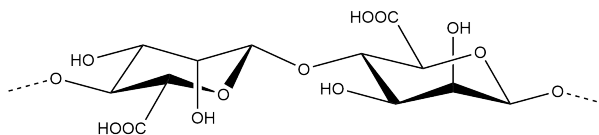


Figure 2.9: Structural formula of the repeating unit of the homopolymer mannuronan, $(1 \rightarrow 4) - \beta$ -D-mannuronic acid.

Mannuronan C-5 epimerase AlgE4 is a modular enzyme consisting of 553 amino acids (aa) divided into a 385 aa A-module, a 142 aa R-module linked by 7 residue linker and terminated by a S-motif [42]. The overall dimensions are $67 \times 37 \times 36$ Å [42].

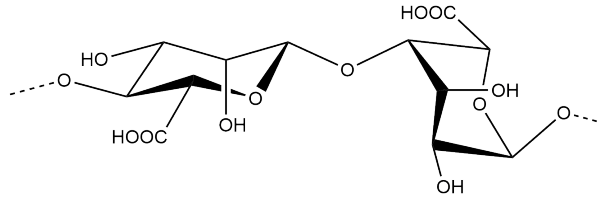


Figure 2.10: The conversion product of AlgE4 acting on the mannuronan precursor, referred to as polyMG. The structure contains alternating monomers of $(1 \rightarrow 4) - \beta$ -D-mannuronic acid (M) and $(1 \rightarrow 4) - \alpha$ -L-guluronic acid (G).

The catalytic activity is effected by the A-module, while the R-module is believed to be regulatory as studies have shown that the R-module has no affinity toward mannuronan [43] [44]. The sequence, found in appendix A.2, includes numerous polar and charged amino acids that may be crosslinked either to carboxyl- or amino groups. A 3D representation with an electrostatic mapping of the entire enzyme can be seen in figure 2.11. While no reference to isoelectric point of AlgE4 have been found in the literature, calculations based on amino acid content indicates an isoelectric point of approximately 4 [45].

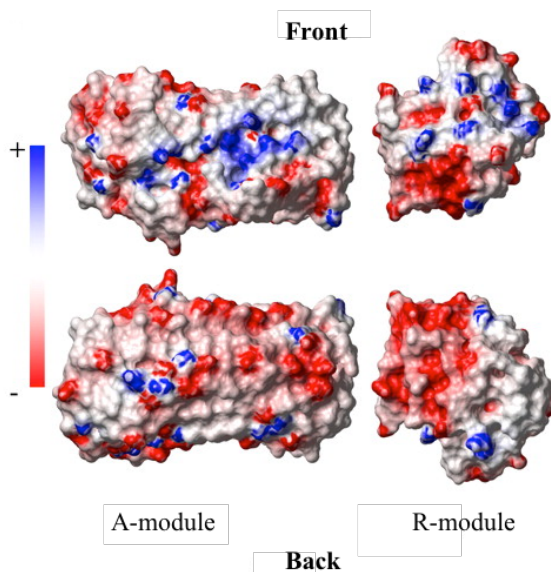


Figure 2.11: Electrostatic potential model of AlgE4, red indicating negative potential and blue positive. Retrieved from [46].

The kinetics of AlgE4 have not been widely studied, but one study suggests that AlgE4 epimerizes mannuronan by a processive mode of action, a single epimerisation taking 0.2 s, though the AlgE4-mannuronan complex having a lifetime of 2.7 s [47]. Another AFM force-rupture study from 2015 supported this, indicating a residence time of 1.7 ± 0.6 s [48]. Both studies were performed at 37 °C, in 20 mM MOPS, 2 mM CaCl₂ and 50 mM HEPES, 10 mM CaCl₂, respectively.

3 | Experimental

This chapter describes the materials, instruments and experimental procedures utilized for the all results included in the thesis. Information is structured on an experiment by experiment basis. The level of detail is intended sufficient for reproduction, while rationale is left for chapter 4, results and discussion.

3.1 Materials

The fluorescent nanoparticles utilized, Thermo Fisher Amine Modified FluoSpheres F8764 and Thermo Fisher Carboxyl Modified FluoSpheres F8811, were delivered as 2 mg/ml colloidal suspensions. They are fluorescent spherical polystyrene particles with a radius of 100 nm, emitting yellow-green fluorescence with an excitation peak at 505 nm and emission peak of 515 nm. The density of surface-bound amine and carboxyl groups was not specified in the documentation from Thermo Fischer and could not be disclosed due to confidentiality concerning the production process. Suspension media was water and sodium azide for bacterial growth prevention. The number of particles per milliliter was calculated to be $4.56 \cdot 10^{12}$ [25].

Mannuronan or polyM with a weight average of 176 kD and polydispersity index 1.8 was produced by an AlgG negative strain of *Pseudomonas Fluorescens* NCIMB 10525 [49]. Mannuronan C5-epimerase AlgE4 with molecular mass 57.7 kDa was isolated from *Hansenula polymorpha* [50]. AlgE4 and mannuronan were kindly provided by Prof. G. Skjåk-Bræk at Dept. of Biotechnology and Food Science at NTNU.

3-Aminopropyl-triethoxysilane (APTES) 99%, hydrochloric acid (HCl) 37%, methanol (MeOH) $\geq 99.8\%$, 1-ethyl-3-(3-dimethylaminopropyl)carbodiimide-HCl (EDAC) 100%, CH_3COOH , phosphate buffered saline tablets (PBS), 4-morpholino-ethanesulfonic acid

$\text{C}_6\text{H}_5\text{NO}_3$ (MES) $\geq 99.5\%$, C-reactive protein 2.1 mg/mL (CRP) and bovine serum albumin 100% (BSA), methoxypolyethylene glycol 5000 (COOH-PEG), O-2-aminoethyl-polyethylene glycol (amin-PEG) and calcium chloride $\text{CaCl}_2 \cdot 2\text{H}_2\text{O}$ were purchased from Sigma-Aldrich. di-natriumtetraborate $\text{Na}_2\text{B}_4\text{O}_7 \cdot 10\text{H}_2\text{O}$ was purchased from Merck KGaA. N-2-hydroxyethylpiperazine-N-2-ethanesulfonic acid (HEPES) was purchased from Merck KGaA.

The PBS buffer solution was prepared to a final concentration of 137 mM NaCl, 2.7 mM KCl and 10 mM phosphate with a pH of 7.4, while MES was prepared to 0.1 M with a pH of 5.5. Boric acid was prepared from di-natriumtetraborate to a concentration of 50 mM, pH 5.8. Acetic acid was prepared to a concentration of 1 mM, pH 5.8. HEPES was prepared individually for each experiment, owing to photo-induced degradation and various concentrations used [51]. The Milli-Q water was produced using Millipore Milli-Q Water Purification System. pH was measured to 7.6 ± 0.2 .

Bath sonication was performed using a Branson 3510 Ultrasonic Cleaner. Sonication at higher intensities was performed with a Bandelin Sonopuls HD310. Eppendorf Centrifuge 5415 R with rotor radius 8.3 cm was used for centrifugation.

Particle analysis with NanoSight Particle Analyzer was carried out at NTNU NanoLab. All other experiments were conducted in the biophysics laboratories in block B4 at the Department of Physics, NTNU.

3.2 Data acquisition

A Zeiss Axio Observer.Z1 inverted microscope with 100X Alpha Plan-Fluar oil immersion objective with a numerical aperture of 1.54 were used for imaging. A field of view of $80 \times 80 \mu\text{m}^2$ was used for every image. For all experiments, filter set with an excitation filter 483 - 493 nm and an emission filter 500 - 550 nm and dichroic mirror at 500 nm were used. The standard fluorescence excitation source was a mercury arc lamp HXP 120 W, while a 25 mW multiline Argon-laser at 488 nm was used for TIRF, with a critical angle of 61.2° . The TIRF angle was measured to be 63.5° , resulting in an evanescent field depth of 140 nm given refractive indices $n_i = 1.518$ and $n_t = 1.330$. [52]. Immersol 518F from Thermo Fischer Scientific with a refractive index of 1.518 was used as immersion oil on the objective. An Andor iXon DU 897BV CCD Camera from Andor Technologies Peltier-cooled to -80°C was used for image acquisition, while the software ANDOR Solis version 4.22 and Zeiss ZEN Blue 2012 were used to control the

ICCD Camera. WillCo Wells 35 mm borosilicate glass slides assembled from part no. KIT-3522 were used as sample holders. Droplets were applied to glass slides with volumes 13-60 μL , depending on the experiment duration, as these volumes made droplets easy to localize and prevented water evaporation to be a factor [53]. PDMS wells were produced at NTNU NanoLab, courtesy of Nina Bjørk Arnfinnsdottir.

A Cypher AFM from Asylum Research with a NANOSENSORS PPP-NCH tip was used with tapping mode in air for AFM images.

3.3 Image analysis

3.3.1 Methodology

Multiple version combinations of java, imageJ and MOSAIC Plugin Suite were used, but for consistency and avoidance of bugs and problems due to version mismatch, java 8 update 144, imageJ 1.50i and MOSAIC plugin suite 1.0.8 were used for all the results included in this report.

In order to make file sizes more manageable and to save processing time, videos were exported in 8-bit greyscale from the TIRF software. For ZEN blue, uncompressed .tif was initially the only export format found to be compatible with MOSAIC. The proprietary Zeiss .czi format was later found to be compatible, and the final AlgE4 mannuronan experiments were saved using this format. For ANDOR, .tif and .sif files were compatible. In cases where the image source was not TIRF data, such as in section 4.1.1, validation and verification, a bug related to the file format handling in MOSAIC caused inversion of the colors. This was circumvented by importing as RGB.

As a first point in the analysis, a histogram of the intensity distribution was generated in Image J in order to verify that the degree of pixel saturation was acceptable and to approximate the intensity threshold for particle detection [54]. The absolute detection threshold parameter was then chosen on the basis of the histogram and the radius based on observed particle size. Detected particles in one frame were considered with the preview function. The absolute threshold was then incremented until all particles in one frame were detected, followed by the repetition across multiple frames, including the last frame. The particle tracking was then initiated with a displacement value equal to the particle radius. Link range was set to 1 for all analysis included herein, with the exception of section 4.1.1. While a larger link range would include particles

with intensity oscillating below the intensity threshold, this was found to include false positives in experiments with large numbers of trajectories. Non-particle discrimination score was also set to 0. Parameters were chosen on the basis that particles of interest are static. The individual detected particles were then inspected by utilizing the GUI to visualize the detected trajectories. If false detections were observed, the threshold was altered. If aggregates were detected, the experiment was repeated unless aggregates were desired. If the same particle was identified as multiple particles due to oscillating intensity, the intensity threshold was lowered. Positions, intensities and particle discrimination scores of the tracked particles were then exported in two .xls files, one containing trajectory data and one with particles bound in less than 2 frames, referred to as segmented data. These were then imported to MATLAB and processed using the custom script detailed in section [A.1](#). Parameters residence times, number of bound particles per frame, cumulative number of bound frames and a measure of the mean grey intensities were extracted by using the MATLAB scripts found in appendix [A.1](#). Dissociation constants were calculated by fitting double exponential fits to residence time distributions as outlined in section [2.2](#) and [4.3.3](#).

3.3.2 Algorithm verification and validation

In order to uncover errors in the image analysis and processing of tracking data, a virtual image sequence was generated and analyzed. This also serves as a demonstration of the functionality of the algorithm. The performance of the particle tracking methodology was further evaluated by reproducing results from Gunnarsson et al. [\[6\]](#). A processing performance benchmark was also performed .

Virtual image sequence

The virtual image sequence created contained 20 frames and was generated using Adobe Photoshop CS5. The image series contained in total 13 object positions of bright spots mimicking fluorescent spheres in a TIRF field of view, shown in figure [3.1](#). The virtual system exhibited customized spatiotemporal properties represented in table [3.2](#), where positions corresponds to the labelled spots shown in figure [3.1](#). The white, grey and black spheres have numerical pixel values of 100, 50 and 0, respectively. Thus, the object with position 1 has pixel values of 100 in frames 1 through 3, 0 in frame 4, 100 in frames 5 to 8, 50 in frame 9 and 100 for the remaining frames. For image analysis,

MOSAIC was initiated with cutoff radius 0.0, absolute threshold 40.0, displacement 2.0, link range 2 and displacement 2.0. The time interval between frames was set to 10 seconds. During the manual analysis representation, intensity values were scaled to fit the value assigned by the computer analysis.

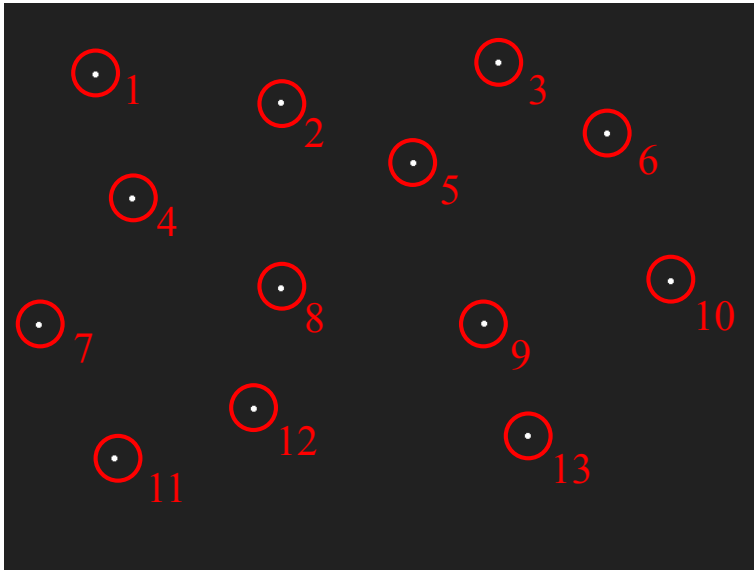


Figure 3.1: Shown is a capture of frame 2 in the digitally generated image sequence used for algorithm testing, every object circled and assigned a position number for transparency.

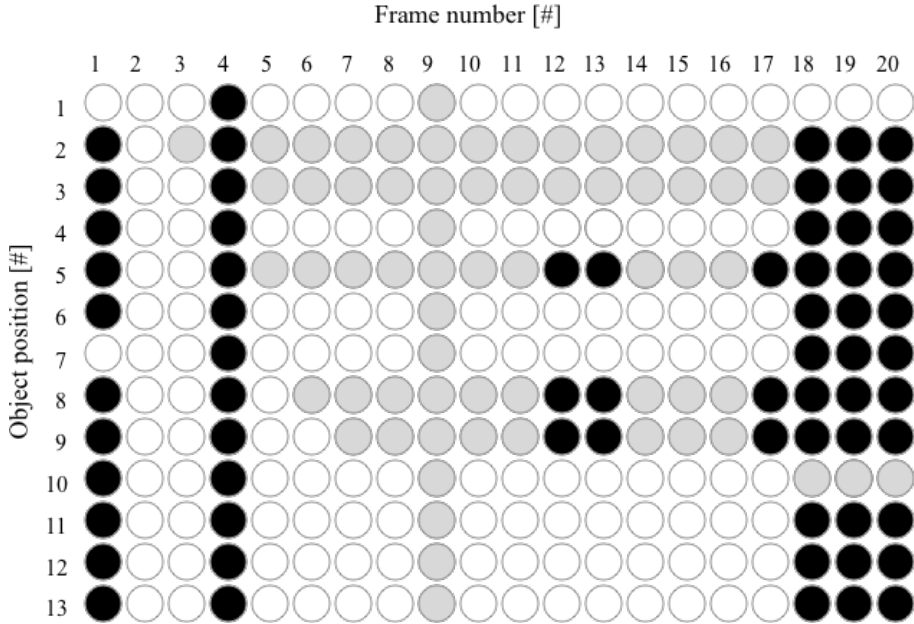


Figure 3.2: A schematic overview of the kinetics of the virtually generated system, the color of each dot indicating the intensity or pixel value of the object in the corresponding frame. Black represents an intensity of zero, grey 50% and white 100%.

Real data reproduction

The published results by Gunnarson et al. in *Nanoletters*, vol. 8, pages 183-188, 2008 exemplified a detection scheme using fluorescently labeled vesicle-DNA-conjugates and a biotinylated surface functionalized with DNA in order to investigate hybridization between a DNA target complementary to both surface bound DNA and vesicle DNA. The material published, 100 fM target detection (filtered), was available in an exotic format (.qt), but could be converted using Quicktime Pro 7.6.6 and exported to uncompressed .tif in 8-bit greyscale for ImageJ and MOSAIC compatibility. Gunnarsson et al. used 0.5 frames per second for data collection, but for the published material half of the frames were removed. MOSAIC's particle tracker was invoked with kernel radius 7.0, cutoff radius 0, percentile 2.0 and displacement 3.0 with a link range of 2. Note that relative percentile was chosen due to low levels of noise and constant brightness across the video.

Processing performance benchmark

Two image series originally generated for fluctuation analysis of mannuran versus AlgE4 (section 4.3.3) were used as example data material. The files were exported from Zen Blue as .czi containing 4807 and 4936 frames, referred to G and H, respectively. The image files were imported to MOSAIC by converting to greyscale and converted to 8-bit. MOSAIC parameters were radius 1, cutoff 0, displacement 1.0, link range 1 and absolute and percentile thresholds 5 and 0.7, respectively. Time was measured using a basic stopwatch and averages calculated on a minimum of two repetitions. The benchmark was performed using OS X 10.13.4 on a 1.7 GHz Intel Core i5-2557M with a multi-core G.-bench score of 3858 [55]. No other processes were active during the benchmark other than a basic LaTeX editor.

3.4 Method development

3.4.1 Assessment of photobleaching

In order to characterize the rate at which fluorescent nanoparticle photobleaching occurred, 4 μL amine functionalized fluorescent NP solution was diluted in 196 μL de-ionized water and vortexed for 30 seconds. 50 μL was applied to an untreated borosilicate glass slide in order for the fluorescent spheres to settle on the glass. The sample was allowed to settle for about 25 minutes before recording was started. Pictures were taken at 5 second intervals over 30 minutes using TIRF at maximum advisable laser intensity, with an exposure time of 4.8 ms and definite focus enabled. ImageJ's Plot Z-axis Profile tool was used to find the mean intensity of each frame for the entire field of view and for regions of interest selected on aggregates to avoid drift to cause single fluorescent spheres to move outside the targeted area.

3.4.2 Separation of aggregates

Six solutions were created in 1.5 mL eppendorf tubes, each containing 51 μg COOH-PEG and 20 μL amine modified fluorescent nanoparticle solution dissolved in 500 μL boric acid and 471 μL MES, following incubation for 15 minutes at room temperature. The COOH-PEG was sonicated separately for 10 minutes prior to addition. 0.2876 mg EDAC dissolved in 29 μL MES and added to each COOH-PEG solution and incubated

for 2 hours at room temperature. Following incubation, the sample was centrifuged at 13200 RPM (rotations per minute) for 10 minutes, the supernatant discarded and replaced with PBS. The pellet was resuspended by repeated triturating, vortexing and bath sonication for 10 minutes. This process was repeated three times. For the final resuspension, MQ-water was added. The particle solutions were centrifuged at 4000, 6000, 8000, 10000 and 12000 RPM immediately prior to imaging. One uncentrifuged sample was kept as reference. Droplets were retrieved from the top of the eppendorf tube and applied to aminosilanized borosilicate glass surfaces. Snapshots were taken with epifluorescence at 0.10 to 2 ms exposure times.

3.4.3 Effect of ionic strength

A buffer of 50 mM HEPES, 10 mM CaCl_2 , pH 6.9 was prepared prior to the experiment and stored protected from light. From this, 15 mL solutions of 1 mM HEPES, 0.2 mM CaCl_2 and 5 mM HEPES, 1 mM CaCl_2 was created. To each of these, a 30 μL carboxylate modified fluorescent nanoparticle solution was added, following vortex and sonication for 10 minutes. Droplets were retrieved from the top of the eppendorf tube and applied to mannuronan functionalized glass slides prepared as detailed in section [3.5.1](#). 10 to 30 minute image series with 2.5 seconds interval and exposure times 30-40 ms were taken in TIRF mode.

3.5 Fluctuation analysis of AlgE4 vs mannuronan

3.5.1 Screening of non-specific surface adsorption

Particle preparation

15 μL carboxylate modified fluorescent nanoparticle solution was dissolved in 15 mL MQ-water following vortexing for 30 s and immersion in an ultrasonic bath for 10 minutes.

Substrate functionalization

Aminosilanized borosilicate glass slides were produced immediately prior to the experiment as detailed in section 3.5.3. The active layers were prepared by dissolving the functionalization compound to be immobilized in a 1:1 solution of 0.1 M pH 5.5 MES and 50 mM pH 5.8 boric acid, incubation for 15 minutes following the addition of EDAC. EDAC was dissolved separately in an identical solution prior to vortexing and immediate addition to the functionalization solution, for the final concentrations shown in table 3.1. 750 μ L of the prepared solution were added to each newly created aminosilanized coverslide, two slides per functionalization for a total of 6 slides. Following incubation, slides with PEG and mannuronan were rinsed thoroughly in MQ-water, while the BSA functionalized slide was rinsed in PBS. The slides were then blown dry using nitrogen. The final four slides with aminosilanization and untreated borosilicate glass surfaces were stored refrigerated in a sealed box during the functionalization.

Surface	Functionalization [g/mL]	EDAC [g/mL]
Glass	-	-
Aminosilanization	-	-
BSA	20	-
Mannuronan	10	1.66
PEG	10	57.5

Table 3.1: Concentrations of the carbodiimide crosslinking agent, EDAC, and the various compounds used for substrate immobilization.

Data acquisition

Functionalized coverslides and samples of functionalized fluorescent nanoparticles were kept at room temperature a minimum of 30 minutes following preparation and imaged in the same day. The fluorescent particles were sonicated in a bath sonicator for 15 minutes and briefly vortexed prior to imaging and applied to coverslides in 15 μ L droplets.

Imaging was initiated immediately following the laser activation and bringing the TIRF in focus. Images were acquired at a rate of 5 frames per second over 20 minutes with periodic focus stabilization. Exposure time was 2-3 milliseconds, with continuous laser illumination of the sample. Each sample was imaged once, the contrast of the images adjusted with ImageJ for visibility.

3.5.2 Mannuronan C5 epimerase AlgE4

Surface functionalization and data acquisition was performed as in section 3.5.1 with the exception that additional 57.5 mg/mL EDAC was used for BSA functionalization.

3.5.3 Fluctuation analysis of AlgE4 vs mannuronan

Particle functionalization

240 μ L carboxylate modified fluorescent nanoparticles were dissolved in 360 μ L 1:1 MES pH 5.5: 50 mM Boric Acid pH 5.8 and vortexed for 30 seconds and distributed equally among six different eppendorf tubes, A to F. 635 μ g EDAC was measured out in 10 mL 1:1 MES pH 5.5: 50 mM Boric Acid pH 5.8. This solution was diluted in series for precision and added to the eppendorfs A - F such that end relative NP:EDAC concentrations were 1:100000, 1:1000, 1:100, 1:10, 1:100 000 and 1:0 respectively. See table 3.2. The solutions were vortexed for 30 seconds and incubated for 30 minutes.

Following incubation, tubes A - D were added 800 μ L AlgE4 in a buffer of 1 mM HEPES, 0.2 mM CaCl_2 , 0.18 ± 0.03 mM Na, giving a total concentration of 0.9 mg/mL AlgE4. Tubes E and F were added the same buffer without AlgE4. HEPES was prepared in MilliQ water two days in advance and stored protected from light at 4°C. pH was adjusted to 6.5 using NaOH, introducing the sodium. The added AlgE4 was dissolved in the buffer for 6 hours on a shaker at room temperature prior to addition. The tubes were incubated overnight on a shaker protected from light at 4°C.

For removal of reaction byproducts and buffer exchange, all samples were centrifuged at 13200 RPM for 10 minutes, the supernatant discarded and replaced with 1 mM HEPES, 0.2 mM CaCl_2 , 0.18 ± 0.03 mM Na. The pellet was resuspended by repeated triturating, vortexing and bath sonication for 10 minutes. This process was repeated three times. Finally, another 1 mL buffer was added.

Substrate functionalization

Substrates of functionalized borosilicate glass slides were produced sequentially, first cleaned by immersion in 1:1 MeOH:HCl for 30 minutes, rinsed with Milli-Q water and blow dried using nitrogen. Aminosilanization was carried out immediately after cleaning

Sample	Fluorescent NP	EDAC	AlgE4	NP:EDAC ratio
A, 2A	$3.3 \cdot 10^{-10}\text{M}$	$3.3 \cdot 10^{-5}\text{M}$	$1.6 \cdot 10^{-5}\text{M}$	100 000:1
B, 2B	$3.3 \cdot 10^{-10}\text{M}$	$3.3 \cdot 10^{-7}\text{M}$	$1.6 \cdot 10^{-5}\text{M}$	1000:1
C, 2C	$3.3 \cdot 10^{-10}\text{M}$	$3.3 \cdot 10^{-8}\text{M}$	$1.6 \cdot 10^{-5}\text{M}$	100:1
D, 2D	$3.3 \cdot 10^{-10}\text{M}$	$3.3 \cdot 10^{-9}\text{M}$	$1.6 \cdot 10^{-5}\text{M}$	10:1
E, 2E	$3.3 \cdot 10^{-10}\text{M}$	0	0	0:1
F, 2F	$3.3 \cdot 10^{-10}\text{M}$	$3.3 \cdot 10^{-5}\text{M}$	0	0:1

Table 3.2: Overview of the particle functionalization reactant concentrations and ratios prior to the purification procedure.

by immersion in 2% APTES in 1 mM acetic acid for 20 minutes, rinsing in Milli-Q water and dried with nitrogen. The slides were then assembled into a glass bottom dish and stored in a sealed box at 4°C.

For the final layer, 4 mg/mL mannuronan was dissolved overnight in 1:1 MES and boric acid. The next day, EDAC in MES and boric acid were added following vortexing and incubation for 15 minutes, bringing the final concentrations of EDAC and mannuronan to 0.9 mg/mL and 3 mg/mL, respectively. 700 μL mannuronan/EDAC solution was applied to each aminosilanized glass bottom dish prepared the previous evening and incubated for 3 hours at room temperature, then at 4°C overnight. Finally, they were rinsed in Milli-Q water, blown dry with nitrogen and stored at 4°C in a sealed box for three days prior to the experiment.

Data acquisition

The TIRF apparatus, laser and associated hardware were turned on four hours prior to imaging in order for the temperature and laser intensity to equilibrate. Functionalized coverslides and samples of functionalized fluorescent nanoparticles were kept at room temperature for at least one hour prior to imaging, protected from contamination and light in a sealed box. Solutions of functionalized particles were sonicated in a bath sonicator for 15 minutes, briefly vortexed and aggregates sedimented by centrifuging at 12 000 RPM for 1 minute 30 seconds immediately prior to imaging. The samples were applied to coverslides in 13 μL droplets.

Imaging was initiated within 1 minute after droplet application, allowing the TIRF laser to be activated and brought into focus. Images were acquired at a rate 5 frames

per second over 20 minutes with periodic focus stabilization. Exposure time was 20 milliseconds, the laser illuminating the sample continuously owing to limitations of the mechanical shutter. Samples were imaged sequentially A-F and 2A-2F, the prefix 2 indicating a repeat on a different coverslide but the same particle batch. The temperature was measured to be 29°C at the TIRF stage prior to imaging sample A and to 31°C after sample 2F. All samples were imaged twice on two different coverslides.

Image analysis

For samples A-F, image analysis was performed enhancing the contrast in imageJ such that 0.01% of the pixels were saturated, allowing every fluorescent object within the evanescent field to be recognized. Then MOSAIC was used for trajectory detection setting radius to 1, cutoff 0, displacement 1 and link range 1. Absolute thresholds were set to between 5 to 9, accounting for difference in intensity, likely due to variations in the functionalization or cover slide thickness. For samples 2A-2F, a percentile threshold of 0.07% was set, removing subjectivity from the analysis.

4 | Results and discussion

This chapter presents the main findings and results for the finalization of the method. The results primarily serve to document and demonstrate a continuous advancement of an original technique; results and discussions are intertwined. For that reason, they are also presented as such. A summary and elaboration of key findings not directly related to any one result is included at the end.

4.1 Image analysis

4.1.1 Algorithm verification and validation

The purpose of this analysis was to ensure there were no bugs or errors in MOSAIC or the subsequent data processing that may consistently cause a misrepresentation of the kinetic parameters. A complete examination required correlating the true kinetic parameters with those acquired through analysis. The virtual image sequence was specifically tailored to reveal potential coding errors, while reproduction of published material gives a measure of the algorithm's performance on real data. The benchmark gives an indication of limitations in the data set size that may be analyzed on a given hardware.

Virtual image sequence

The table was manually processed, frame by frame, as this was the only mean to extract the kinetics. During this process, the rules of the algorithm detailed in section 2.5 and A.1 were applied. As follows, trajectories with objects detected in the first or last frame were filtered from the residence time distribution, and objects with identical positions in two frames separated by a single frame were mapped into a single trajectory. The cumulative number of bound objects included only one detected bound object per trajectory. The number of bound objects and mean grey intensity includes all detected objects stationary for a minimum of two frames.

The results of this process are represented by the red graphic shown in figures 4.1 (a) - (d), while the blue graphic shows the corresponding results using the computer algorithm developed. As manual computation is prone to human error, 3.2 in section 3.3.2 may also be assessed for verification. This overview also helps demonstrate properties of the algorithm; a link range of 2 caused the particles not detected at $T=40$ s to be part of the same trajectory due to having the same position. It is worth noting that the mean grey intensity calculated in figure 4.1 corresponded to the detected objects, thus only considering objects with intensities above the detection threshold. This is embodied by the discontinuity at $T=40$ s. The arbitrary max mean intensity value of 7.8 was allocated by the image conversion in ImageJ.

In summary, the detection and extracted parameters match exactly the kinetics of the system, confirming that the algorithm contains no errors.

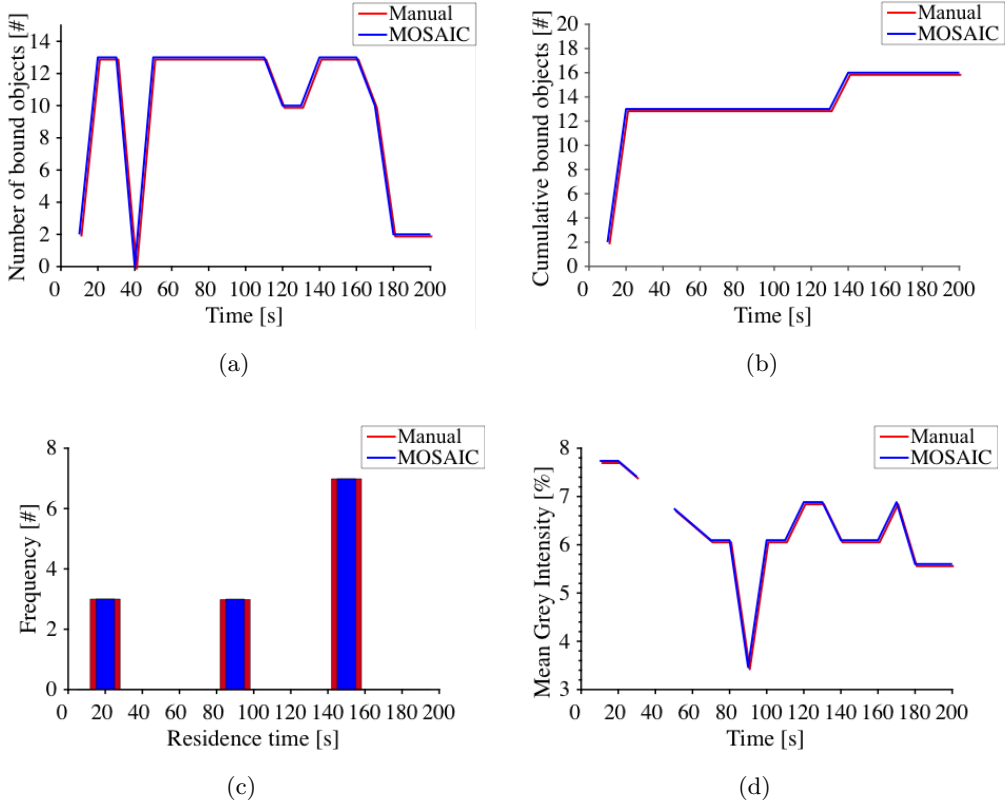


Figure 4.1: Data extracted from the processed image sequence. (a) Number of detected objects vs time. (b) Curve indicating the cumulative number of bound objects mapped into trajectories. Contrasted with (a) allows distinguishing trajectories with intensities dipping below detection threshold from new arrivals. (c) Represents extracted residence times in which objects present in the first frames are filtered. (d) Mean intensities of detected objects, indicating if drift of focus or bleaching could influence the analysis. Juxtaposing with figure 3.2 shows accordance, indicating no errors in the algorithm.

Real data reproduction

Figure 4.2 shows the number of bound vesicles per $90 \times 90 \mu\text{m}^2$ as detected by MOSAIC versus the MATLAB based algorithm used by Gunnarson et al. [6]. While other findings in the report could be compared, they are all derived from this data with assumptions that are not fully transparent. Thus, the number of bound vesicles per frame serves as the best basis for comparison. It is evident that the numbers of detected bound vesicles

closely resemble over the entire experiment. Until frame 150, the curves completely overlap, after which the MOSAIC based approach at any time detects 1-2 additional vesicles. Visual inspection of the source video revealed that the additional vesicles identified are either faint or in the near vicinity of another vesicle. Exemplified in figure 4.3, the boxed four particles in the lower middle to right side of the image are either faint or in close proximity, making it possible that these are the additional vesicles tracked by MOSAIC. It can be contended whether these should be accepted as detections of vesicles or not. All in all, the analysis points toward that the methodology using imageJ and MOSAIC gives results comparable to what was reported. As a side note, the videos retrieved were subject to a low-pass filter, removing noise and making detection simpler. Applying the method to data derived from videos recorded with a different setup may yield different results.

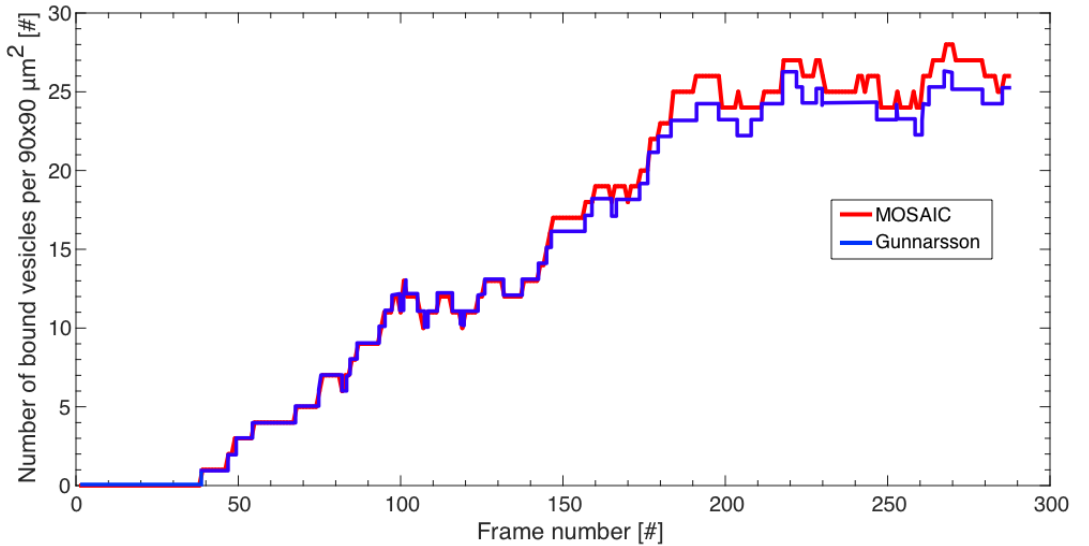


Figure 4.2: Plot of the number of bound vesicles as recognized by the particle tracking algorithm developed in this project (MOSAIC) and the MATLAB procedure used by Gunnarsson et al. [6].

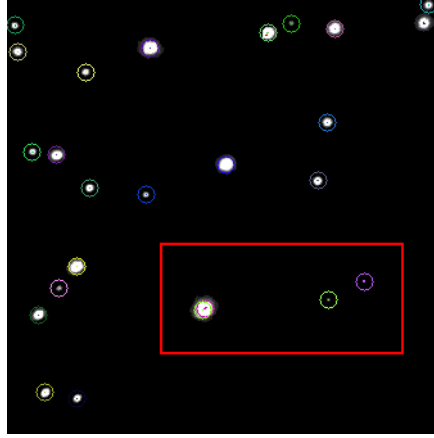


Figure 4.3: Shown is a snapshot of the particle detection preview of MOSAIC at frame 212 of the data from Gunnarsson, detected particles labelled with colored circles. Candidates for the additional particles detected by MOSAIC are boxed in red.

Processing performance benchmark

Processing time using MOSAIC and the MATLAB programmed data analysis scripts on the preprocessed 8-bit greyscale .czis resulted in the processing times shown in table 4.1. The detection data extracted from the two image series with MOSAIC was composed of 42664 and 597164 rows of trajectory data, respectively.

Data	Trajectory data points [#]	MOSAIC time [s]	MATLAB time [s]
G	42664	117	11
H	597164	121	2465

Table 4.1: Overview of the average processing times in MOSAIC and MATLAB for two distinct data sets of different size, based on a minimum of two repetitions.

MOSAIC processing time remained relatively constant despite large variations in the number of data points extracted. As MOSAIC works through the frames sequentially, only considering two frames at a time given a link range of 1, a larger number of detections do not significantly increase processing time. The subsequent MATLAB processing relies on multiple conditional for loops, causing the processing time to increase at a rate more than proportional to the data set size. This makes data sets of greater size impractical to work with. To note is that it is likely possible to increase the efficiency of the scripting by more than two-fold by programming optimization.

4.2 Method development

In the experimental part of the project, severe problems were encountered with the stability of the functionalized fluorescent nanoparticles. Irreversible binding, sedimentation and aggregation were observed. Attempted solutions included varying conjugation chemistry, sonication, centrifugation and different purification protocols. Since the technique is highly sensitive to sedimentation and aggregation, this was the major setback. Throughout this process, in excess of 120 surface functionalization processes were carried out since February. A number of different particle functionalizations were also carried out. Eventually it was found that, despite manufacturer claims, the fluorescent nanoparticles used were stable only at ionic strengths of several millimolars and below [56]. Here are included the experiments of public interest and important for the realization of the method.

4.2.1 Assessment of photobleaching

Photobleaching would cause a gradual decrease of the average intensity, possibly causing the intensity of fluorescent spheres to drop below the threshold of the algorithm. Figure 4.4 (c) shows the mean gray value of the entire field of view as shown in figure 4.4 (a) plotted against frame number. The intensity is fluctuating, and more interestingly, gradually increasing at a near linear rate until around frame 330. This is contrary to what would be expected if bleaching occurred, and unexpected. Deposition of more fluorescent spheres on the surface, lateral drift causing spheres to move out of the field of view or change in focus could explain this observation.

Further confining the region analyzed to pixels part of fluorescent clusters, shown in figure 4.4 (b), yields the intensity plot shown in figure 4.4 (d). Here, the mean intensity remains relatively constant until frame 200, after which the intensity decreases linearly. This is inconsistent with the results for the entire field of view. However, by reviewing the time lapse and noting the exact positions of the fluorescent sphere clusters, it is possible to discern a slight drift of the entire observed area, likely due to mechanical drift in the system. As this makes the bright spots move out of the analyzed regions pixel-by-pixel, a sudden drop is expected.

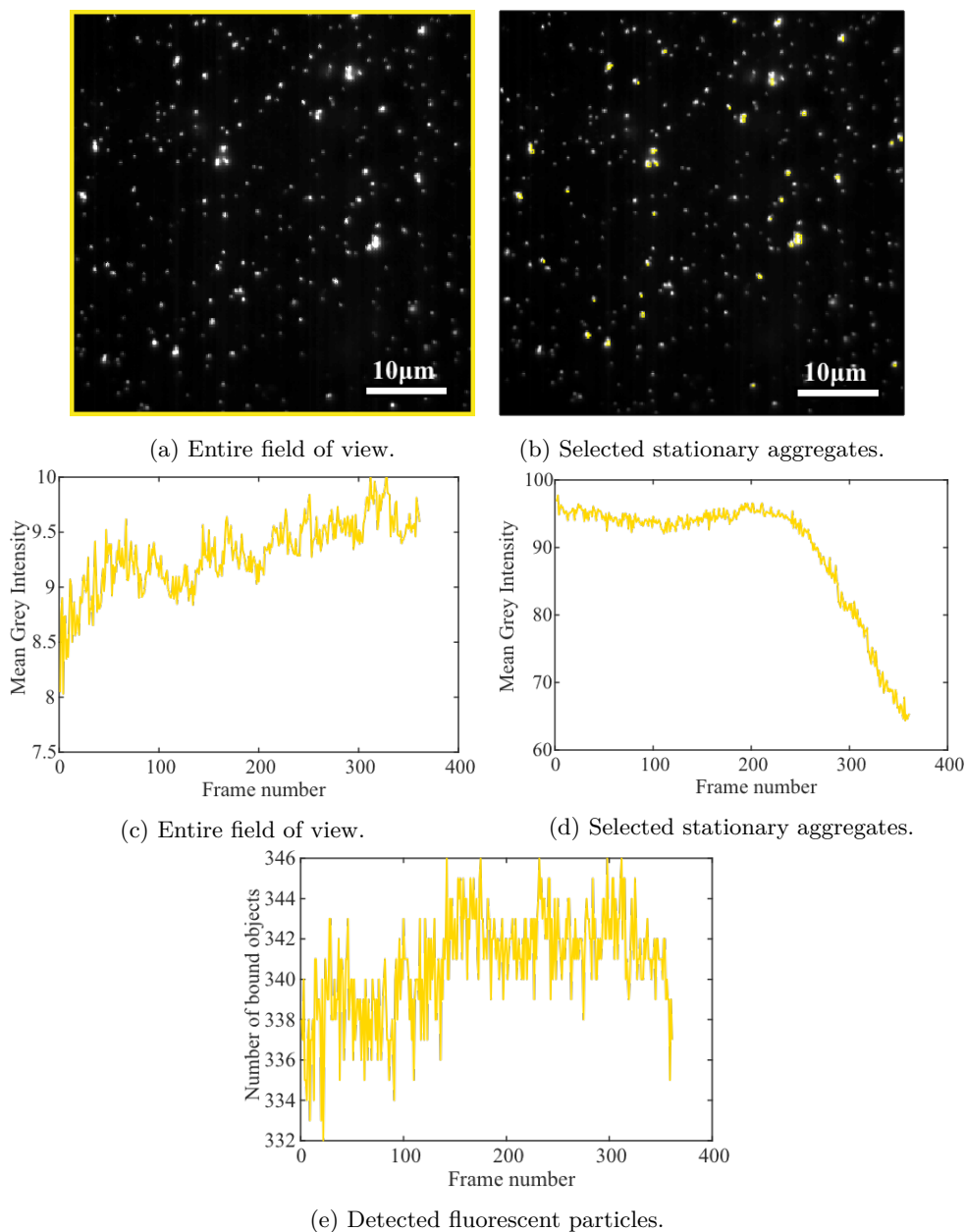


Figure 4.4: (a) and (b) shows TIRF micrographs of unfunctionalized amine fluorescent nanoparticles on substrate of untreated borosilicate coverslides, the yellow regions illustrating the areas used for the mean gray value measurements. (c) and (d) shows mean gray values for the respective areas. (e) shows the algorithm's number of detected objects per frame. The images were acquired over a 30 minute time lapse with 5 second image intervals and exposure time 4.8 ms.

Figure 4.4 (e) shows the number of spheres as detected by the MOSAIC particle tracker, fluctuating between 332 and 348. The number is slightly increasing over the time frame, yet again contrary to what would be observed if photobleaching occurred, but explaining some of the intensity increase for the entire field of view. A slight drop is seen from roughly frame 300 and onward. This is a relatively small decrease and may be due to drift of focus or fluorescent spheres moving out of the field of view, but coincides with the slight intensity decrease found in figure 4.4 (c).

As such, there is little indicating that photobleaching occurs at a rate that should influence analysis over time scales and exposure rates used, though it is also revealed that mechanical drift can obscure measurements. Note that for experiments using continuous laser exposure such as those in section 4.3.3, the exposure rates can be magnitudes higher. To alleviate this problem, a script was written to obtain the mean grey intensity of detected particles, included in appendix A.1. It would also be possible to filter out trajectories in which the intensity gradually decreases below a set value.

4.2.2 Separation of aggregates

Aggregation was an inherent property of the polystyrene-based particles, observed following every particle functionalization performed. The algorithm was highly sensitive toward aggregates, due to noise and large intensity variations causing false detections. Furthermore, aggregates show different dynamics, diffusing slower and sedimenting at a significantly higher rate than single particles. Thus, removing aggregates prior to analysis was of paramount importance.

Several approaches for redispersion and filtering were attempted and discarded, including centrifugal filters, dialysis, probe sonication and ultracentrifugation. NanoSight Particle Analysis system was also used during this process, but found to be imprecise owing to the appropriate laser being out of order.

Of primary importance for the separation of aggregation was found to be a simple centrifugal separation at medium speed immediately prior to imaging. Figure 4.5 shows epifluorescence micrographs of carboxyl functionalized fluorescent particles saturated with PEG and centrifuged for 90 seconds at various speeds. The uncentrifuged reference sample in (a) exhibits aggregation to an extent that fluorescence background originating outside the focal plane causes lens flare in the optics. Exposure rate was decreased to reduce this. At lower RPM, (b) - (e), aggregates are still apparent, although

the absence of lens flare signifies some sedimentation. Figure 4.5 (f), displays a clear improvement at 12000 RPM, with zero aggregates in plain view and no background fluorescence. No higher rotation speeds were explored, as 12000 was sufficient to achieve monodispersity in the upper section of the eppendorf tubes from which particle samples were extracted.

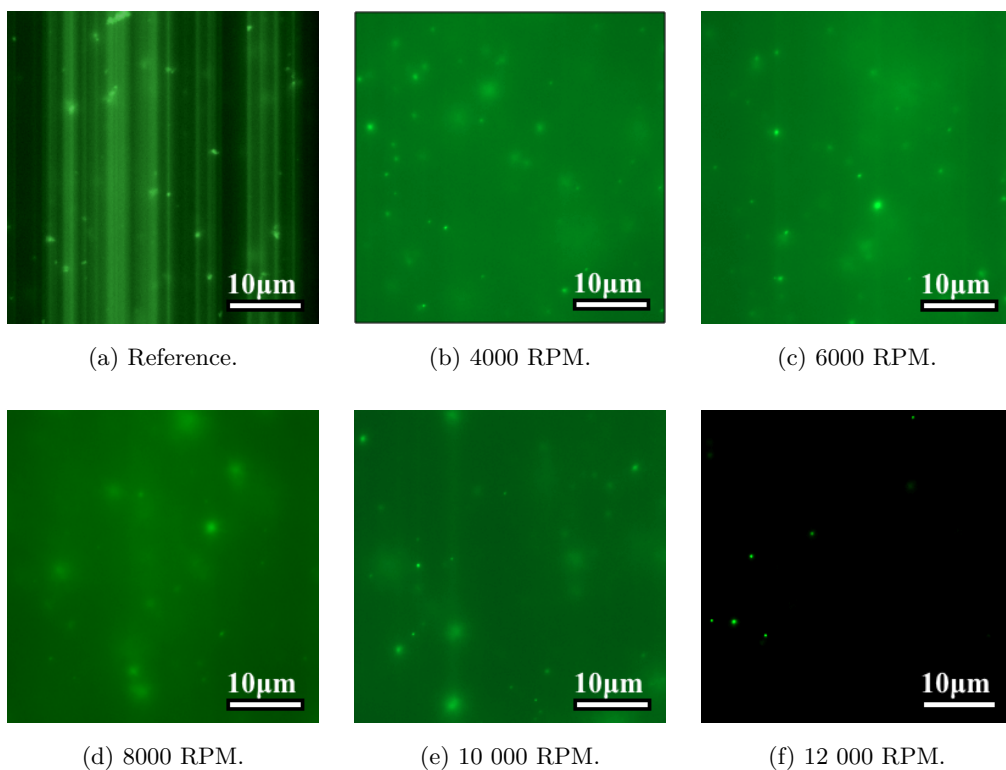


Figure 4.5: (a) - (f) shows epifluorescence micrographs of 2% PEG functionalized fluorescent amine NPs in MQ-water, where aggregates were sedimented at specified rotations per minute over 90 seconds.

4.2.3 Effect of ionic strength

As the influence of buffer solution was explored in an early phase prior to the optimization of experimental parameters required for monodispersity, the effect of the ionic strength was long believed not to be of importance. In support of this were also manufacturer claims of stability at ionic strengths up to 200 mM [56].

Surprisingly, TIRF micrographs in figure 4.6 shows an undeniable correlation between ionic content and dispersity of the carboxyl functionalized NPs. The TIRF micrograph in (a), shows only two objects bound within the field of view for deionized MQ-water. At 1 mM HEPES, 0.2 mM CaCl_2 , in (b), the difference in surface affinity is discernible. In (c), at 5 mM HEPES, 1 mM CaCl_2 , it is unambiguous. Interestingly, at higher ionic concentrations, as shown in (d), aggregation is observed; the particles aggregate at a rate such that few single particles are seen bound at the interface. This attests that electrostatic forces are essential not only for colloidal stability, but also for non-specific surface adsorption. While evident that Ca^{2+} and Cl^- compresses the electrostatic double layer, HEPES might also be absorbed at the particle interface, neutralizing the charge [57] [58]. The individual contributions of HEPES and CaCl_2 were not pursued in the following. All this necessitates that fluctuation analysis experiments using the fluorescent NPs take place at ionic conditions at which they are stable in solution. Though, it also shows the magnitude of the non-specific interaction of the fluorescent NPs to be significant.

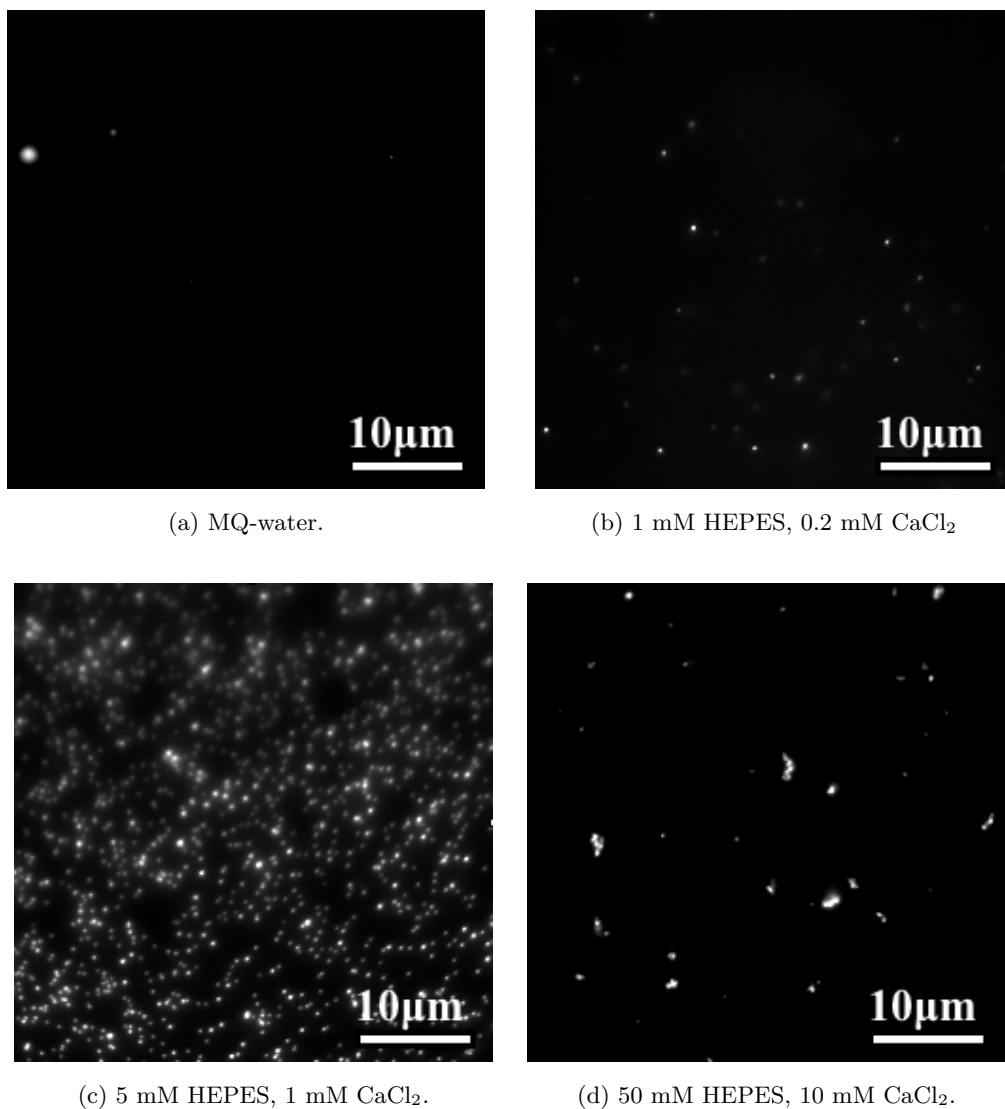


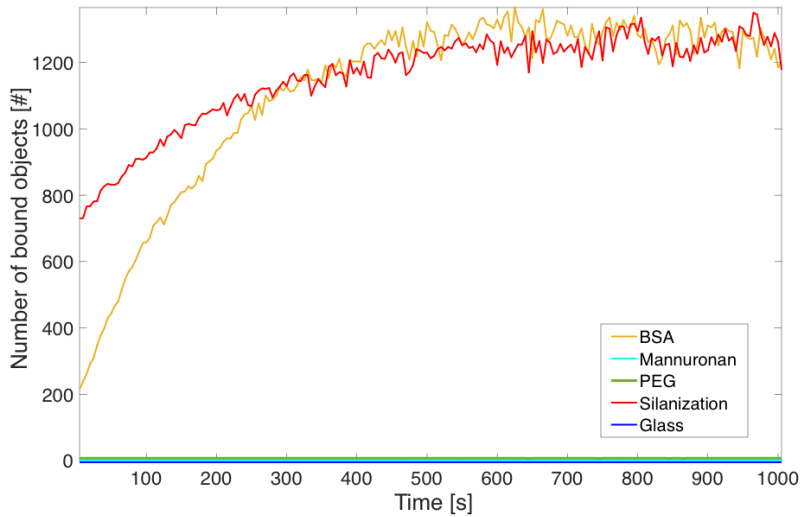
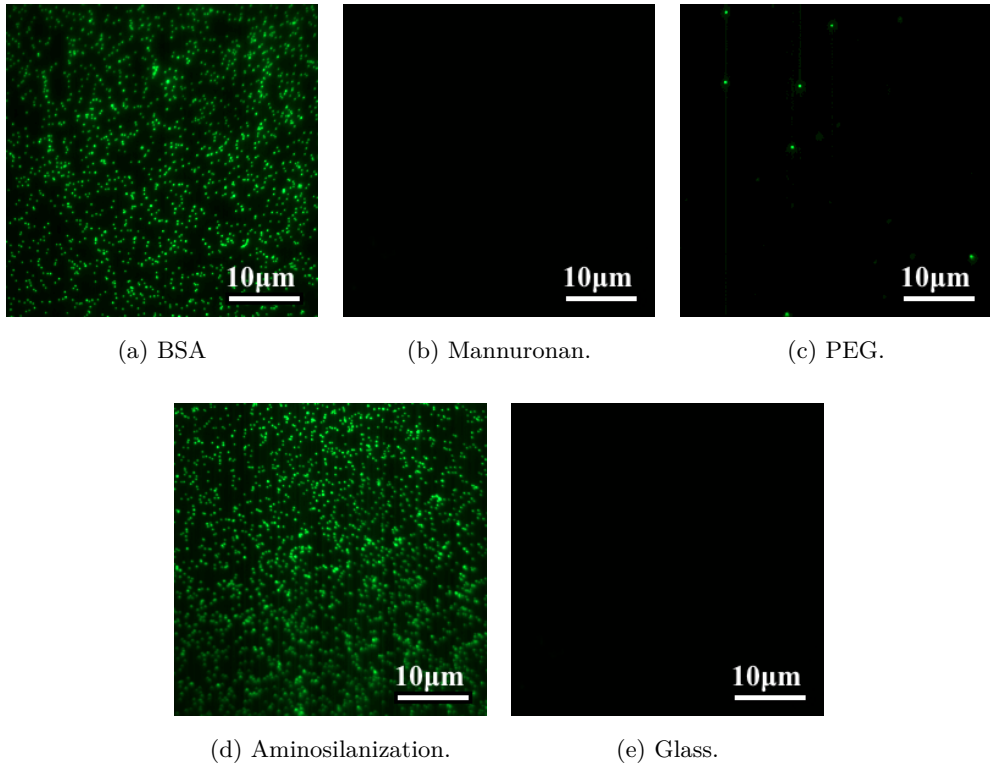
Figure 4.6: TIRF micrographs of various buffer concentrations with 0.2% carboxyl functionalized fluorescent NP solutions on borosilicate coverslips functionalized with mannuronan on aminosilanization. Snapshots taken 10 minutes after droplet deposition.

4.3 Fluctuation analysis of mannuronan vs AlgE4

4.3.1 Screening of non-specific surface adsorption of carboxyl functionalized fluorescent nanoparticles

The characterization of the non-specific binding between carboxyl NPs and various interfaces was a requirement in order find a suitable surface passivation layers and as a control experiment. This would allow differentiation between unfunctionalized and AlgE4 functionalized carboxyl nanoparticles against mannuronan and other surface compositions. Furthermore, shedding light on the interplay between fluorescent polystyrene nanoparticles and various interfaces was of interest.

The five surfaces, BSA, PEG, mannuronan, aminosilanization and untreated glass, have different charge, composition and topography. Glass served as a control experiment and reference, while the remainder were of interest due to suitability as passivation layers. The carboxyl functionalized spheres were expected to hold a negative charge in water or buffers with pH around 7 due to deprotonation of carboxyl groups of pKa 2-5 inducing a negative surface charge [59]. Previous work has suggested zeta potentials of -36 and -55 mV reinforcing this, and indicating electrostatic interactions to be a possible driving force for colloidal stability but also for adsorption to positively charged surfaces [60] [61].



(f) Number of bound objects.

Figure 4.7: (a) to (e) shows TIRF Micrographs taken 1000 s after deposition of 0.1% unfunctionalized carboxyl NPs in MQ-water on the surfaces indicated in subcaptions. (f) shows the corresponding number of detected bound object plotted against time.

Figure 4.7 (a) - (e) shows the surface bound objects deposited on the functionalized surfaces over 1000 s, while number of bound objects plotted against time is seen in 4.7 (f). APTES is covered with surface bound NPs. This is unsurprising, as the surface-bound amine groups on APTES contributes to a positive surface charge and has been reported to have a pKa of 10 [62]. More interestingly, the coverslip saturated with BSA displays similar saturation. This can not be attributed to purely electrostatic interactions, as BSA has an isoelectric point around 5, resulting in an overall negative charge at pH 7 [63]. While BSA has domains of positive charge, it is much smaller than the fluorescent particles in all dimensions and would in any case lead to a significantly lower deposition rate [64]. Furthermore, BSA is commonly used as a blocker, serving to decrease the non-specific binding to various surface compositions [65]. On this background, it is reasonable to assume that the surface coverage of BSA is not sufficient to screen the aminosilanization's positive charge. It is also possible that rinsing in PBS or immersion in MQ-water caused desorption of BSA.

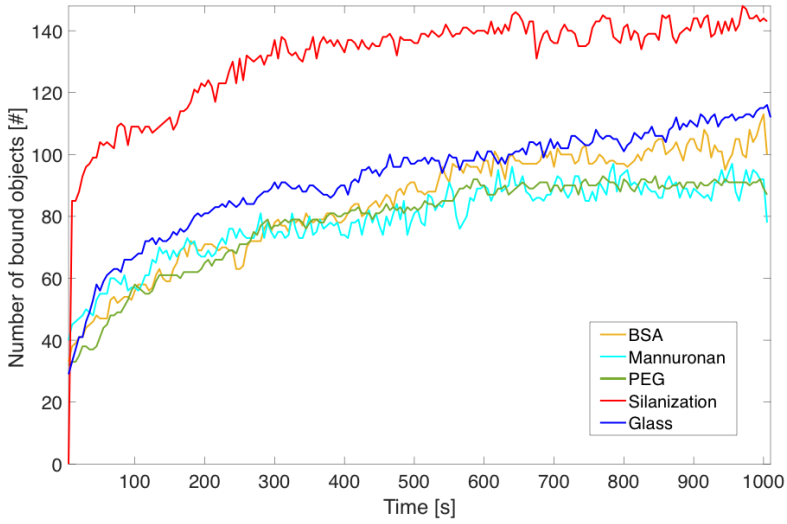
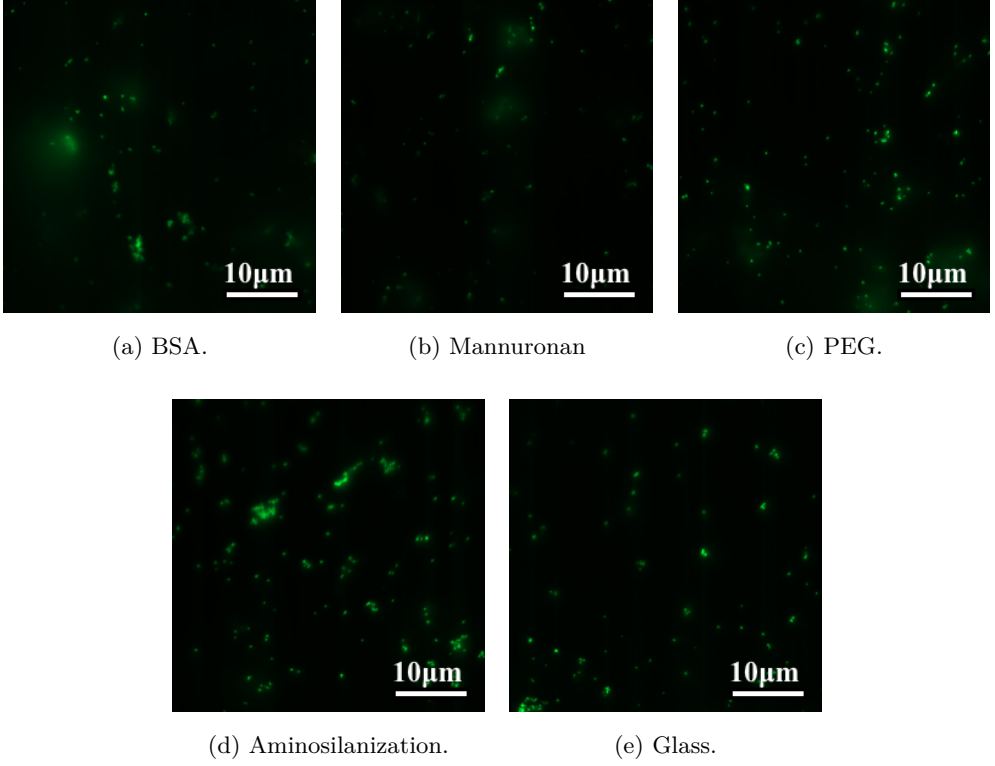
The remaining three surfaces exhibited zero or low degrees of non-specific binding. The NPs showed no affinity to the activated glass surface in accordance with the negative charge induced through the dissociation of terminal silanol groups [66]. PEG also showed a very low rate of binding, though as represented in figure 4.7 (c), a few NPs were bound to the surface for the entire duration of the experiment. PEG is often cited to be neutral [67], but in reality holds a slight negative charge in water [68] [69]. The binding observed may be attributed to incomplete surface coverage or PEG failing to completely screen the positive charge of the underlying aminosilanization. This observation has also been made by several others, who have found multi-step functionalization and use of additional blockers such as polyoxyethylene sorbitan monolaurate to improve surface passivation [70] [71]. This could be an option, if the need to use PEG as a passivation layer arose. Finally, for mannuronan, no binding was observed for the entire 20 minutes. This is in line with a reported pKa of 3.38 [72]. Furthermore, as no particles adsorb, complete surface coverage is implied. What is more interesting, is as zero unspecific binding was observed between carboxyl nanoparticles and mannuronan, the strategy of utilizing a low surface density of AlgE4 on carboxyl NPs presented itself, avoiding using any complicating passivation layers.

4.3.2 Mannuronan C-5 epimerase AlgE4

Mannuronan and its C-5 epimerase AlgE4 is assumed to form a complex with a lifetime of approximately 2 seconds at 37 in HEPES. As such, experiments could be carried out at more practical time scales at which problems due to evaporation or instrumental failure should be surmountable. Furthermore, acquiring sufficient statistics should be possible even with a low amount of fluorescently labeled conjugates, allowing less material to be spent per experiment. Following an insight from Prof. Stokke and Senior Engineer G. Maurstad, mannuronan was used for surface immobilization only, owing to its abundant and readily accessible COOH-groups. These are prone to crosslinking and formation of covalently linked aggregates. AlgE4 on the other hand, would only be targetable at the surface terminal amino groups of lysine. As multivalent binding was expected using high surface densities on both fluorescent NPs and coverslips, the effect of different surface chemistries had to be examined, following immobilization with a low density of mannuronan such that multivalent interactions could be minimized. It was initially believed that aminosilanization would have low affinity or no affinity toward AlgE4, as this was not cited in previous work, which would greatly simplify the optimization of surface coverage, only having to vary the density of mannuronan without worrying about a passivation layer [48].

Shown in figure 4.8 (a) - (e) are micrographs at $T = 500$ s after deposition for the relevant surface chemistries. Unexpectedly, AlgE4 showed affinity toward all surfaces, rendering the initial strategy of simply lowering the surface density void. Moreover, analysis utilizing MOSAIC indicates AlgE4's specific binding rate toward mannuronan to be lower than the unspecific interactions [48]. As follows, each and every surface chemistry investigated are inapplicable as passivation layers for AlgE4-conjugated NPs. (Note that the discontinuity at the onset of the aminosilanization curve is due to the block plate on the laser not being removed for the first image.)

Conjugating blockers mixed in with AlgE4 is a poor endeavour, as carboxyl and amine groups on AlgE4 also would be targeted by the blocker, altering the properties of the protein.



(f) Number of bound objects for all surfaces.

Figure 4.8: (a) - (e) shows TIRF micrographs of Alge4 fluorescent NPs in 50 mM HEPES, 10 mM CaCl_2 on the surfaces specified 500 s after deposition. (f) shows the number of detected bound objects plotted against time for the various surfaces.

4.3.3 Fluctuation analysis of mannuronan vs AlgE4

Sample	Fluorescent NP	EDAC	AlgE4	NP:EDAC ratio
A, 2A	$3.3 \cdot 10^{-10}\text{M}$	$3.3 \cdot 10^{-5}\text{M}$	$1.6 \cdot 10^{-5}\text{M}$	100 000:1
B, 2B	$3.3 \cdot 10^{-10}\text{M}$	$3.3 \cdot 10^{-7}\text{M}$	$1.6 \cdot 10^{-5}\text{M}$	1000:1
C, 2C	$3.3 \cdot 10^{-10}\text{M}$	$3.3 \cdot 10^{-8}\text{M}$	$1.6 \cdot 10^{-5}\text{M}$	100:1
D, 2D	$3.3 \cdot 10^{-10}\text{M}$	$3.3 \cdot 10^{-9}\text{M}$	$1.6 \cdot 10^{-5}\text{M}$	10:1
E, 2E	$3.3 \cdot 10^{-10}\text{M}$	0	0	0:1
F, 2F	$3.3 \cdot 10^{-10}\text{M}$	$3.3 \cdot 10^{-5}\text{M}$	0	0:1

Table 4.2: Overview of the particle functionalization reactant concentrations and ratios prior to the purification procedure. NP:EDAC ratio theoretically determines number density of covalently bound AlgE4 per NP.

Each particle functionalizations were imaged twice on different substrate functionalizations to shed light on potential variations in surface topography and composition, and reveal major experimental errors. Temperature and pretreatment of solutions and buffers were precisely controlled in order to minimize the chance of unknown variables influencing the experiment. HEPES is subject to photo-induced degradation, requiring it to be freshly prepared or protected from light during storage [51] [73]. The buffer concentration used was high enough for AlgE4 enzyme activity, yet low enough to allow the fluorescent NPs to be stable in solution.

The literature shows that EDAC generally has been used in ratios 50-3000:1, EDAC to protein [48] [47] [74] [75] [76] [77] [35]. Here, a different approach using AlgE4 in excess while controlling the amount of EDAC was attempted. It was expected that using discrete EDAC to NP ratios and varying the EDAC amount, the average surface density of conjugated AlgE4 could be controlled. The multivalency would result in an inverse correlation between dissociation constant and EDAC concentration [78]. As EDAC should react one-to-one with carboxyl groups, forming an intermediate with a half life of several hours at pHs 5-6, incubating the carboxyl-NPs prior to the addition of AlgE4 should be a viable strategy [79] [37] [80]. As EDAC has been found to destabilize electrostatically stabilized colloids, aggregation rate might also be affected [81] [82]. This approach was also supported by the carboxyl group activation forming the O-Acylisourea intermediate being most effective at acidic conditions, while the substitution reaction is commonly cited to be more effective at basic conditions [81]. This kept AlgE4 at more ideal buffer

conditions, making denaturation of the enzyme less likely. Furthermore, using low rates of EDAC should reduce the chance of selfpolymerization between amine and carboxyl groups rendering the biomolecule inactive [81]. In short, the procedure used in this final experiment should offer an improvement over previous approaches. While the effectiveness of these adaptations preferentially should have been explored individually, only time and material for a single particle functionalization was available.

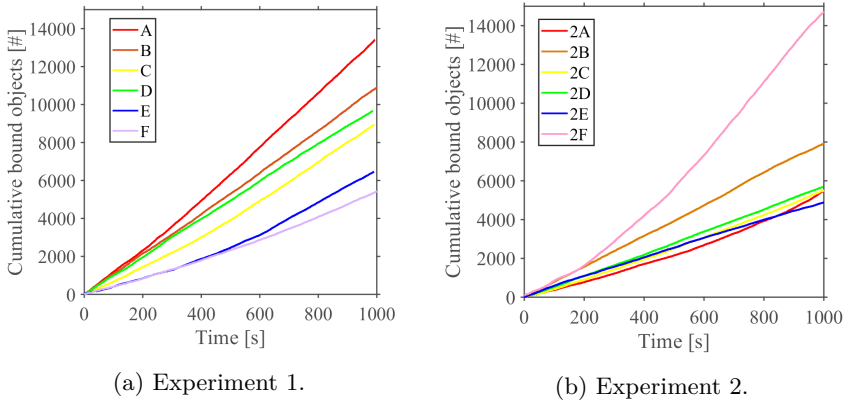


Figure 4.9: Shown is the cumulative number of bound particles for the two experiments. A - F denotes particle functionalizations of varying AlgE4 densities, detailed in table 4.2.

Figure 4.9 shows the cumulative number of bound particles detected for the various surface densities, each count corresponding to a new trajectory. As can be verified by the residence times in section A.3, the majority are short trajectories representing unbound, freely diffusing particles being recognized across multiple frames due to randomness. As such, particle concentration and effective depth of the evanescent field are likely key parameters affecting the total count. The slope of the curve gives more information regarding the kinetics of the system. Assuming equilibrium conditions, association and dissociation rates should be constant, resulting in a linear curve. A convex curve would imply deposition on the surface inhibiting further binding or depleting the functionalized NPs in the solution. A concave curve could indicate false detections due to aggregates or intensities fluctuating around the detection threshold, though could also be due to a sedimentation profile developing as outlined in section 2.3.4. The total counts are all in the range 4800 to 14600 for 2E to 2F, respectively. Alternating the detection thresholds with ± 2 for a single sample gave a difference in particle counts of $\leq 20\%$,

meaning the difference was largely due to actual sample variations and not disparity in the analysis. The first experiment shows direct correlation between the expected AlgE4 surface density on the nanoparticles and cumulative number of bound particles and concave curves. This could infer that particles with higher AlgE4 surface densities show higher affinity, possibly due to compression of the electrostatic double layer or weak specific binding. However, no such tendency was found in the second experiment. The second experiment also shows near-linear development for curves 2A, 2C, 2D and 2E. This could be attributed to the percentile based threshold, preventing bound, bleached particles from fluctuating below threshold limit, but could also be due to the percentile threshold algorithm favoring detecting a constant number of particles per frame. 2E and 2F in particular shows a significantly larger number of detections. This observation was verified by visually going through the video and varying threshold parameters. This was attributed to variations in surface topography and composition, introduced in the functionalization or due to degradation during storage, demonstrating that sample to sample variations may significantly influence particle binding.

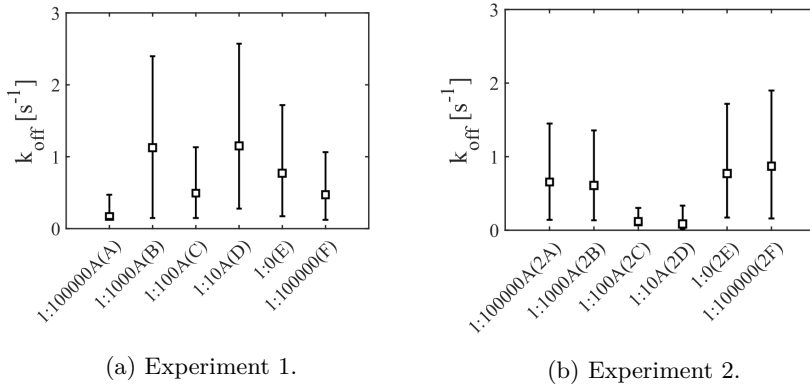


Figure 4.10: Scatter plots of the calculated dissociation constants based on a Langevin model of binding for two independent experiments. Under the assumption unbound particles followed Fickian diffusion, a two term exponential was fitted to the residence time distributions to retrieve k_{off} . The error bars indicate the bounds of the 95% confidence interval. The residence distributions are found in appendix, section [A.3](#)

Figure [4.10b](#) shows the dissociation constant for the specific interaction between the functionalized particles with different surface densities of AlgE4. The residence times

follows an exponential distribution as derived in equation 2.6. A double exponential was used for fitting by nonlinear least squares method in MATLAB, in which one term accounted for random detections of freely diffusing particles and one accounted for the specific interactions from which k_{off} was extracted. While the number of detections varies, embodied by the difference in cumulative number of bound particles, this should lead to a count increase for all binding events and not change the shape of the distribution. As follows, this would be represented in a change in the prefix of the exponential term and not the exponent. In consequence, the dissociation constant should be unaffected.

Despite the trajectory data containing thousands of trajectories, uncertainties are significant across all samples, k_{off} varying from 0.03 to above 2.5 s^{-1} . Furthermore, no correlation between surface density of AlgE4 and k_{off} can be seen. No specific binding can be discerned through the commotion of randomly diffusing particles and non-specific binding. As even AlgE4 saturated NPs can not be distinguished from the untreated control, using a more precise mathematical model to better filter these events would be futile. Increasing the amount of statistics by increasing particle count or experiment length also holds little promise, as this would increase non-specific binding and random detections. Experiments of much longer lengths would also be impractical due to the duration of both the experiment and subsequent analysis.

The effectiveness of the final particle functionalization strategy was not explored, though even given zero covalently bound AlgE4, a degree of physisorption would be expected. Given this, E, 2E, F and 2F should show different dissociation constants, as here no AlgE4 was available in solution for physisorption. The mannuronan surface functionalization has also not been explored, and may change properties following immobilization and exposure to air. Keeping the mannuronan functionalized surface immersed in liquid could be an improvement in this respect.

4.4 Substrate functionalization characterization

While investigation of the surface functionalization was not within the scope of this project, examining the topography of the mannuronan functionalized borosilicate glass slides used in section 4.3.3 was of interest. This could explain the variations in kinetics observed for particles with identical functionalization.

Figure 4.11 shows height profile and phase shift AFM images of the mannuronan func-

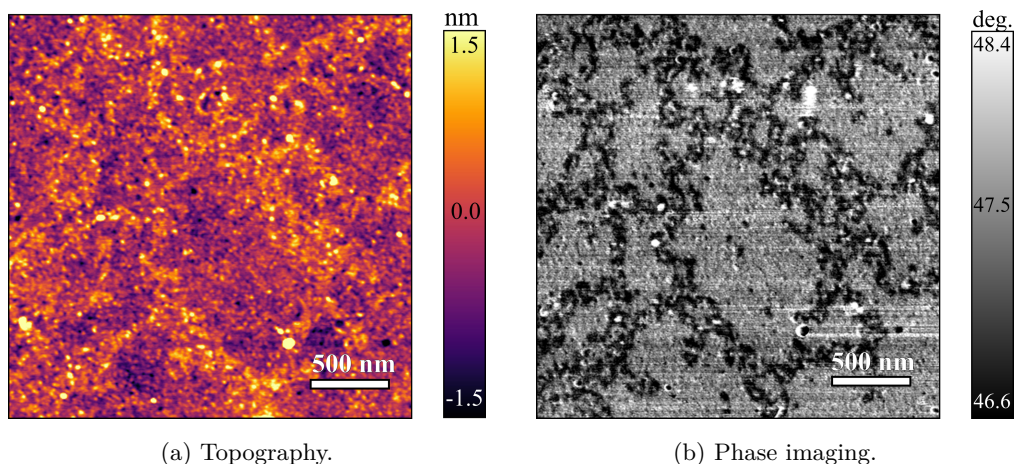


Figure 4.11: Tapping mode AFM images of borosilicate glass slides aminosilanized with 2% APTES in 1 mM acetic acid for 20 minutes, functionalized with 3 mg/mL mannuronan and 0.9 mg/mL EDAC for 2 hours. AFM instrumentation with assistance from Nina Björk Arnfinnsdottir.

tionalization used throughout the project. As mannuronan has no amine groups, a monolayer of mannuronan with some islands of aggregates would be expected. The height profile indicates a relatively even surface, varying only with 3 nm within the field of view. However, this does not exclude the possibility that the lower sections are aminosilanization, while the higher features represent mannuronan. The phase image offers more information regarding the composition. Here two distinct areas with a phase shift of 1.8 degrees are observed, pointing toward the bright fields in 4.11 (a) and dark fields in 4.11 (b) representing mannuronan and the lower regions aminosilanization. Taking into consideration results from section 4.3.1, in which carboxyl particles was found to show zero binding to a similar surface, a complete surface coverage would be expected as otherwise the aminosilanization would be available for binding. This could be explained by mannuronan behaving differently in solution, polymers uncoiling on the surface, neutralizing the positive charge of the aminosilanization and preventing binding. A more thorough examination and optimization of the substrate functionalization would be of interest, and could be a necessity for acquiring surfaces with reproducible properties.

4.5 Viability of method

In this section, the viability of the experimental framework utilized during this project in light of findings in the literature and expertise gained throughout the experimental process are discussed. The image analysis is not included, as it is detailed in section [4.1.1](#).

As has been observed, the polystyrene nanoparticles used as fluorescent probes rely on electrostatic stabilization due to hydrophobicity and disposition for non-specific binding. This not only limits the solution conditions to buffers of low ionic strength, but may also affect the activity and conformation of the conjugated biomolecules. Others have also noted that the fluorescent NPs made out of polystyrene have a significant surface roughness of polymers extending from the particle surface [\[83\]](#) [\[84\]](#). As the fluorescent NPs are magnitudes larger than the protein, it follows that interaction energies are also likely larger; any fingerprint of the particle is likely to be significant. While non-specific interactions of polystyrene NPs have been noted in the literature, no reference to fluctuation analysis could be found [\[60\]](#). This supports a claim that the polystyrene NPs are unsuitable for fluctuation analysis. Relating this to the methodology of Gunnarsson et al., these concerns were largely nullified by using lipid vesicles [\[6\]](#). Lipid vesicles have an hydrophilic exterior, are largely uncharged and have a mass density matching the aqueous solution. Thus, the natural environment of the conjugated macromolecules is closely mimicked. It would be highly interesting to simply replace the fluorescent particles studied herein with an alternative probe of smaller fingerprint, such as the novel zwitterionic NPs only recently described in Nature Methods [\[85\]](#).

The vesicles also offer the advantage that both well-established biomolecular modification schemes and kinetic parameters are available [\[6\]](#). In the present study, potential complications are related to both crosslinking chemistry and biomarker-particle interface. Proteins may change conformation in response to hydrophobic and charge surface properties [\[86\]](#) [\[87\]](#). Challenges have also been found by others related to both activity and stability of conjugated functional groups [\[88\]](#). The kinetics of the crosslinking reaction in response to various chemical parameters are also not completely understood [\[78\]](#). Gunnarsson et al. instead used a non-covalent avidin-biotin binding for the immobilization of the functional groups, which have different shortcomings [\[89\]](#). EDAC offers advantages in the stability of a covalent bond, versatility in conjugation chemistry and relative simplicity of the chemical species involved. Furthermore, the EDAC conjugation strategy utilized herein, using discrete EDAC to biomolecule ratios, alleviates many

of the specified issues. EDAC is also a mainstay for biosensor surface immobilization tissue and extracts [90].

Whereas the immobilization chemistry has precedence, the interaction of the immobilized macromolecules AlgE4 and mannuronan has only been explored at NTNU [47] [74] [48]. Thus, some uncertainty is associated with the kinetic parameters. Additionally, the shortness of the hypothesized value of around 2 s increases the difficulty of filtering out random detections of freely diffusing particles with low affinity. Gunnarsson et al. studied only biomolecules for which the kinetic parameters were known. This allowed significant simplification of the analysis by only considering trajectories with residence times within a set time interval.

5 | Conclusion

The goal of the project was establishing a method for the extraction of single-molecule fluctuation parameters using fluorescent polystyrene nanoparticles of radii 100 nm and TIRF. To that end, a theoretical and experimental framework was devised supported by an algorithm for the extraction of fluctuation parameters from spatiotemporal observations. The assay was demonstrated by characterizing the interaction of surface-bound polysaccharide polymannuronan and nanoparticles functionalized with its C5 epimerase AlgE4.

The algorithm showed consistence in the extraction of kinetic parameters from both results published in the literature and a virtually generated image sequence. Residence times, dissociation constants, number of bound particles and a measure of photobleaching was retrieved and represented. The algorithm also proved to be capable of analyzing in excess of 40000 trajectory data points over 5000 frames within minutes. Thus, the algorithm is capable of retrieving correct kinetic parameters from data sets large enough to be of statistical significance.

For the substrate and particle functionalization, the carbodiimide crosslinking chemistry strategy used by the biosensor group at NTNU was adapted and advanced. Various particle and substrate functionalization schemes were explored as candidates for kinetic experiments and passivation layers. Difficulties due to prevalence of non-specific binding and aggregation was experienced; no separation method or passivation layer was found appropriate.

Varying ionic concentration revealed the fluorescent polystyrene NPs' hydrophobic properties and reliance on electrostatic stabilization to be the driving force for both non-specific binding and aggregation. In light of this, electrostatic stabilization was utilized by surface and particle immobilization of the negatively charged macromolecular pair

mannuronan and its C5 epimerase AlgE4. The ionic strength was kept at a minimum, and aggregates separated out. The characterization of the interaction revealed that the fingerprint of the fluorescent nanoparticles was of such a magnitude that the AlgE4-mannuronan interaction could not be discerned. No correlation between nanoparticle surface density of AlgE4 and affinity or residence time could be found; the experiment serves primarily as a demonstration of the capability of the methodology.

While the fluorescent nanoparticles were concluded to be inapplicable, the method holds promise. In relation to the procedure of Gunnarsson et al., using vesicles and a biotin-avidin based binding protocol, more stability and versatility is gained with carbodiimide crosslinking chemistry. Although vesicles offer clear advantages in dispersity and established biomolecular conjugation schemes, more preparation and research infrastructure are required. As the functionalization scheme of the present study may readily be adapted, replacing the fluorescent nanoparticle should be trivial. It is expected that utilizing recent advents of highly dispersible fluorescent nanoparticles with a small fingerprint would allow the realization of a versatile assay with single-molecule sensitivity [85].

Further Work

Apart from replacing the fluorescent probe used, the methodology could be improved in several respects. This section presents suggestions for further work in an eventual continuation of the project.

- Characterizing and verifying the carbodiimide crosslinking protocol employed. Employing Quartz Microbalance for reaction study and chromatography for relating particle mobility to number of functionalized groups. Zeta potential measurements could likely also be employed to this end.
- Characterization of substrate functionalization, particularly for characterizing variations in topography and thickness. AFM for topography, FIB or SEM for cross-sectional imaging.
- Increase the ease-of-use of the data analysis. Convert the data processing to a javascript ImageJ-compatible plugin. Incorporate the fitting of double exponentials into the automated analysis for easier retrieval of dissociation constants.
- Expand functionality of the script with particle size analysis capabilities based on relating tracked motion to diffusion constant.
- Incorporate filtering of photobleached fluospheres as well as detection of freely diffusing particles or non-specific interactions.

Tips and tricks

- Dividing experiments into several recordings allows processing to be completed with low performance CPUs.
- Convert to 8-bit within imageJ to speed up processing at the loss of intensity resolution.
- Exporting experiments as .czi is compatible with ImageJ, allowing for easier file handling and quicker processing.
- Exporting configuration in ImageJ allows reaffirming that analysis parameters were correctly set.
- More RAM and CPU threads may be activated in options. Note that it is possible to set the limit higher than the available internal memory. This is required for large data sets, though will be very slow unless used in conjunction with a solid state drive.
- Using a plastic tweezer is key in order to avoid breaking slides during cleaning and functionalization.
- Assessing pellet size following centrifugation allows quick way of assessing concentration.
- 15 μ L droplets evaporates within roughly 30 min on the TIRF stage. Choose droplet sizes according to experiment length.
- Storing solutions and coverslides cold and protected from contamination is essential, due to bacterial growth and the surfaces high sensitivity to contamination.
- If problems are experienced with the definite focus, restarting ZEN Blue usually resolves the issue. Otherwise a full hardware reset is required. In experiments

lasting over 20 minutes, restarting between each experiment decreases chance of failure.

- Experiments with duration up to several days may be performed using PDMS wells to encapsulate the sample and preventing evaporation and contamination.
- If definite focus is set to periodic stabilization, a bug disallows acquisition rates above roughly 1.5 FPS. This may be circumvented by disabling the period stabilization, only setting time point stabilization. A slight frame drop may be experienced, so as few as possible time points should be used.
- The ANDOR software allows for higher resolution and more advanced camera settings, though turned out to be incompatible with definite focus.
- Convenient resources exist for helping find optimal centrifugation speeds for sedimentation and purification [\[91\]](#).

A | Appendix

A.1 Scripts for data analysis

MATLAB code to process the raw data exported from MOSAIC.

```
%Black Sheep Wall TIRF v1.05 - Written by Are Bruvold. (15.03.2018)
%-----
%SEE BELOW FOR USER SET PARAMETERS
%-----

%Program for filtering and graphically representing kinetic parameters
%from image series of TIRF micrographs.
%Dependant on ImageJ and MOSAIC to extract particle trajectories.
%Program capabilities:
% o Graphically representing:
%     - Distribution of residence times.
%     - Number of bound objects plotted against time.
%     - A measure of bleaching by plotting Mean Intensity against time.
%     - Cumulative number of arrived objects.
% o Filters objects bound at experiment start and end.
% o Control of filtered particles at start and end by storing discriminated
%   objects in the variables n0 and ne.
% o Relative equilibrium constant, giving a measure of particles in the
%   vicinity of surface, yet not binding.
% o Accomodates easy to follow storage of experiment parameters and generated
% data.
```

```

%-----

% GUI FOR DATA SELECTION AND STORAGE
fprintf('Choose first directory in which data will be saved,')
fprintf('\n')
fprintf('then the location of the trajectory data file')
fprintf('\n')
fprintf('and finally the segmented particles export from MOSAIC.'
fprintf('(.csv, .txt or .xls all supported formats')
default_dir=uigetdir(); %Choose the directory for storage.
[maindat,PathName] = uigetfile('*.','Select the trajectory export' ...
    'from MOSAIC',default_dir);
if maindat==0
    return
end
[segdat,PathName] = uigetfile('*.','Select the segmented particles' ...
    'export from MOSAIC',default_dir);
if segdat==0
    return
end

%-----

%FILE FORMAT PROCESSING
%ImageJ exports raw data with extension .xls, though in actuality
%NOT microsoft excel. maindat is the export of the detected trajectories,
%while segdat is the export of the segmented objects.
%MOSAIC output needs to be changed to .txt to be handled by matlab,
%which the followinh section of code handles.
copyfile(num2str([default_dir '/' maindat]), num2str([default_dir '/' ...
    'maindat.txt']));
copyfile(num2str([default_dir '/' segdat]), num2str([default_dir '/' ...
    'segdat.txt']));
maindat=readtable(num2str([default_dir '/' 'maindat.txt']));
segdat=readtable(num2str([default_dir '/' 'segdat.txt']));

```

```

mdat=table2array(maindat);
sdat=table2array(segdat);

%-----

%USER SET PARAMETERS: To be set prior to processing.
dt=0.2; %frame interval [unit: s]. This is also for graph formatting.
et='5'; %exposure time [unit: ms] for imaging.
imode='tirf'; %specify if epi or TIRF mode used.
analysisdate=clock; %obtains the date at which the analysis was performed.
experimentdate='0523'; %date [MMDD] at which the experiment was performed.
experimentname='FSC 1mM HEPES 220A, take 2'; %name of experiment: for storage.
surface='200A-mann'; %surface analysed.
particle='FSC+AlgeE4C1 1 MM HEPES CCLEAN'; %particle functionalization used.
MOAIC='radius:1, cutoff:0, abs.threshold:72, displacement:1, link range:1';

%-----

%Code stubs required for program function
n=max(mdat(:,3)); %total number of frames minus one.
t_exp=dt*(n+1); %recording time/ duration of experiment.
n0=0;
ne=0;

%-----

%NUMBER OF BOUND OBJECTS PER FRAME
%Number of frames particles are detected stored in dat(:,3).
%Create vector "eqb" with size equal to # frames. Note that imageJ uses 0
%as index for first frame. Note that if below detection threshold, the traj
%will NOT be included: Eg. if a particle part of a trajectory is below
%detection threshold for a single frame, but the link range allows the
%trajectory to continue, it will NOT be registered as bound for that frame.
totframes = (n+1);
eqb=zeros(1,(totframes));
for i = 1:length(eqb)

```

```

eqb(i)=sum(mdat(:,3)==(i-1));
end

%-----

%CUMULATIVE BOUND OBJECTS
%counts cumulatively the arrival of particles at the surface. Note that
%this is based on the trajectories.
trapp=zeros(1,totframes);
trapp((mdat(1,3)+1):totframes)=trapp((mdat(1,3)+1):totframes)+1;
for i = 2:size(mdat(:,2),1)
    if mdat(i,2)~=mdat(i-1,2)
        trapp((mdat(i,3)+1):totframes)=(trapp((mdat(i,3)+1):totframes)+1);
    end
end

%-----

%Mean Intensity
%Gives an indication of bleaching, creating a vector with the mean
%intensity of the detected object per frame. Position in vector is frame
%number, value is mean intensity.
MI=zeros(1,(n+1));
for i=1:size(mdat,1);
    MI((mdat(i,3)+1))=MI((mdat(i,3)+1))+mdat(i,7);
end
MI=MI./eqb;

%-----

%RESIDENCE TIMES
%Acquires the residence times or # frames a particle is stationary/bound.
%Creates vector with size # of total trajectories. Inserts the residence
%time for each trajectory at at position in vector according to trajectory
%identity.
res=zeros(1,max(mdat(:,2)));

```

```

q=mdat(1,3);
for i = 2:size(mdat(:,2),1)
    if mdat(i,2)~=mdat(i-1,2)
        res(mdat(i-1,2))=mdat(i-1,3)-q;
        q=mdat(i,3);
    end
    if i==size(mdat(:,2),1)
        res(mdat(i,2))=mdat(i,3)-q;
    end
end

%-----

%FILTERING OF RESIDENCE TIMES
%Filters trajectories of particles bound in the first and last frame of
%the time series. Stores trajectories filtered in n0 and ne, respectively.
for i = 1:size(mdat(:,2),1)
    if mdat(i,3)==0
        res(mdat(i,2))=0;
        n0=n0+1;
    end
    if mdat(i,3)==(n)
        res(mdat(i,2))=0;
        ne=ne+1;
    end
end

%-----

%RELATIVE EQUILIBRIUM CONSTANT
%An attempt to get a measure of particles binding rate relative to observed
%nonbound objects. ( k_rd=[L]/[LR] )
k_rd=(size(sdat,1)/size(mdat,1));
%-----

%PLOTS AND EXPORT OF VECTORS AND USEFUL VARIABLES TO MATLAB WORKSPACE

```

```

set(0, 'DefaultLineLineWidth', 2);
set(0, 'defaultAxesFontName', 'Times New Roman')
set(0, 'defaultTextFontName', 'Times New Roman')
figure(1)
plot(trapp, 'Color', [0 0 1]);
set(gca, ...
    'Box'          , 'off'          , ...
    'TickDir'      , 'out'          , ...
    'XMinorTick'   , 'off'          , ...
    'YMinorTick'   , 'off'          , ...
    'YGrid'        , 'off'          , ...
    'XColor'       , [.3 .3 .3], ...
    'YColor'       , [.3 .3 .3], ...
    'YTick'        , 0:(roundn(max(trapp),1))/10:(roundn((max(trapp)+5),1)), ...
    'XTick'        , 0:round(size(eqb,2)/10):size(eqb,2) , ...
    'LineWidth'    , 1.5            , ...
    'FontSize'     , 21);
xtk = get(gca, 'XTick');           % Converts frame # to time
xtklbl = xtk * dt;                 % by multiplying /w 'dt' and
set(gca, 'XTick', xtk, 'XTickLabel', xtklbl) % Replacing 'XTickLabel' values.
xlabel('Time [s]', 'FontSize', 22)
ylabel('Cumulative bound objects [#]', 'FontSize', 22)
savefig(num2str([default_dir '/' experimentdate experimentname ...
    '_cumbound' '.fig']));
set(1, 'units', 'centimeters', 'pos', [0 0 16 11])
screenposition = get(gcf, 'Position');
set(gcf, ...
    'Name', num2str([experimentdate experimentname '_cumbound']), ...
    'PaperPosition', [0 0 screenposition(3:4)], ...
    'PaperSize', [screenposition(3:4)], ...
    'Position', [10 25 screenposition(3:4)]);
print(1, '-painters', num2str([default_dir '/' experimentdate experimentname ...
    '_cumbound']), '-dpdf')
%
figure(2)

```

```

plot(eqb, 'Color', [0 0 1]);
set(gca, ...
    'Box'          , 'off'          , ...
    'TickDir'      , 'out'          , ...
    'XMinorTick'   , 'off'          , ...
    'YMinorTick'   , 'off'          , ...
    'YGrid'        , 'off'          , ...
    'XColor'       , [.3 .3 .3], ...
    'YColor'       , [.3 .3 .3], ...
    'LineWidth'    , 1.5            , ...
    'FontSize', 21);
xTk = get(gca, 'XTick')      ;           %Converts frame # to time
xTkLbl = xTk * dt;          ;           %by multiplying /w 'dt' and
set(gca, 'XTick', xTk, 'XTickLabel', xTkLbl) %Replacing 'XTickLabel' values.
xlabel('Time [s]', 'FontSize', 22)
ylabel('Number of bound objects [#]', 'FontSize', 22)
%title(num2str([experimentdate experimentname '_nbound'])) optional
savefig(num2str([default_dir '/' experimentdate experimentname '_nbound' ...
    '.fig']));
set(2, 'units', 'centimeters', 'pos', [0 0 16 11])
screenposition = get(gcf, 'Position');
set(gcf, ...
    'Name', num2str([experimentdate experimentname '_nbound']), ...
    'PaperPosition', [0 0 screenposition(3:4)], ...
    'PaperSize', [screenposition(3:4)], ...
    'Position', [26 25 screenposition(3:4)]);
print(2, '-painters', num2str([default_dir '/' experimentdate experimentname ...
    '_nbound']), '-dpdf');
edges=[1:100]-0.5;
%
figure(3)
histogram(res, edges, 'FaceColor', [0 0 1], 'FaceAlpha', 1);
set(gca, ...
    'Box'          , 'off'          , ...
    'TickDir'      , 'out'          , ...
    'XMinorTick'   , 'off'          , ...

```

```

'YMinorTick' , 'off' , ...
'YGrid'      , 'off' , ...
'XColor'     , [.3 .3 .3] , ...
'YColor'     , [.3 .3 .3] , ...
'LineWidth'  , 1.5 , ...
'FontSize', 21);
xTk = get(gca, 'XTick') ;
xTklbl = xTk * dt; ;
set(gca, 'XTick', xTk, 'XTickLabel', xTklbl)
xlabel('Residence time [s]', 'FontSize', 22)
ylabel('Frequency [#]', 'FontSize', 22)
num2str([experimentdate experimentname '_MeanIntensity']);
savefig(num2str([default_dir '/' experimentdate experimentname '_restimes' ...
    '.fig']));
set(3, 'units', 'centimeters', 'pos', [0 0 16 11])
screenposition = get(gcf, 'Position');
set(gcf, ...
    'Name', num2str([experimentdate experimentname '_ResTimes']), ...
    'PaperPosition', [0 0 screenposition(3:4)], ...
    'PaperSize', [screenposition(3:4)], ...
    'Position', [10 10 screenposition(3:4)]);
print(3, '-painters', num2str([default_dir '/' experimentdate experimentname ...
    '_restimes']), '-dpdf');
%
figure(4)
plot(MI, 'Color', [0 0 1]);
set(gca, ...
    'Box' , 'off' , ...
    'TickDir' , 'out' , ...
    'XMinorTick' , 'off' , ...
    'YMinorTick' , 'on' , ...
    'YGrid' , 'off' , ...
    'XColor' , [.3 .3 .3], ...
    'YColor' , [.3 .3 .3], ...
    'XTick' , 0:round(size(eqb,2)/10):size(eqb,2) , ...
    'LineWidth' , 1.5 , ...

```



```

    'FontSize', 21);
xstk = get(gca, 'XTick')    ;
xtklbl = xstk * dt;        ;
set(gca, 'XTick', xstk, 'XTickLabel',xtklbl)
xlabel('Time [s]', 'FontSize', 22)
ylabel('Mean Grey Intensity [%]', 'FontSize', 22)
savefig(num2str([default_dir '/' experimentdate experimentname ...
    '_MeanIntensity' '.fig']));
%title(num2str([experimentdate experimentname '_MeanIntensity'])) optional
num2str([default_dir '/' experimentdate experimentname '_MeanIntensity' ...
    '.fig']));
filename=num2str([experimentdate experimentname]);
set(4, 'units', 'centimeters', 'pos', [0 0 16 11])
screenposition = get(gcf,'Position');
set(gcf,...
    'Name',num2str([experimentdate experimentname '_MeanIntensity']),...
    'PaperPosition',[0 0 screenposition(3:4)],...
    'PaperSize',[screenposition(3:4)],...
    'Position',[26 10 screenposition(3:4)]);
print(4,'-painters',num2str([default_dir '/' experimentdate experimentname ...
    '_MeanIntensity']),'-dpdf');
fid=fopen(num2str([default_dir '/' experimentdate experimentname]),'a');
%Following section exports essential parameters to a .txt file.
fprintf(fid,'Date of analysis: %.0f%.0f%.0f%.0f%.0f%.0f\n', fix(clock));
fprintf(fid,'Date of experiment: %s\n', experimentdate);
fprintf(fid,'Name of experiment: %s\n', experimentname);
fprintf(fid,'Surface: %s\n', surface);
fprintf(fid,'Particle: %s\n', particle);
fprintf(fid,'MOSAIC parameters: %s\n\n', MOSAIC);
fprintf(fid,'Image mode: %s\n', imode);
fprintf(fid,'Experiment duration: %.0f\n', t_exp);
fprintf(fid,'Frame interval: %.2f\n', dt);
fprintf(fid,'Exposure time: %.2f\n\n', et);
fprintf(fid,'Relative equilibrium constant %.4f\n', k_rd);
fprintf(fid,'ne %.0f\n', ne);
fprintf(fid,'n0 %.0f\n\n', n0);

```

```

fprintf(fid, '-----\n\n');
fclose(fid);
clearvars maindat segdat i q n PathName Screenposition xtk xtkbl ...
    analysisdate ans et fid tirf filename default_dir%cleans up variables
return

```

A.2 Protein sequences

```

MDYNVKDFGALGDGVSDDRASIQAAIDAAYAAGGGTVYL
PAGEYRVSAAGEPGDGCLMLKDGVYLAGAGMGETVIKL
IDGSDQKITGMVRSAYGEETSNFGMRDLTLDGNRDNTSG
KVDGWFGYIPGGDGADRDVTIERVEVREMSGYGFDPH
EQTINLTIRDSVAHDNGLDGFVADYLVDSVFENNVAYAND
RHGFNVVTSTHDFVMTNNVAYGNGSSGLVVQRGLEDLAL
PSNILIDGGAYYDNAREGVLLKMTSDITLQNADIHGNGSSG
VRVYGAQDVQILDNQIHDNAQAAVPEVLLQSFDDTAGA
SGTYYYTTLNTRIEGNTISGSANSTYGIQERNDGTDYSSLID
NDIAGVQQPIQLYGPSTVSGEP

```

Figure A.1: Representation of the amino acid sequence of the Mannuronan C-5 epimerase A-module [92].

```

GSDGEPLVGGD TDDQLQGGSGADRLDGGAGDDILDGGA
GRDRLSGGAGADTFVFSAREDSYRTDTAVFNDLILDFEAS
EDRIDLSALGFSLGDGYGGTLLLKTNAEGTRTYLKSFEA
DAEGRRFEVALDGDHTGDLAANVVFAATGTTTELEVLG
DSGTQAGAI V

```

Figure A.2: Representation of the amino acid sequence of the Mannuronan C-5 Epimerase R-module [92].

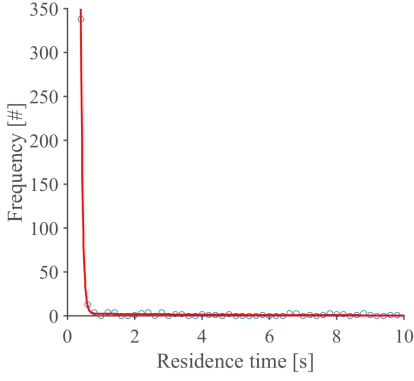
```

MDYNVKDFGALGDGVSDDRASIQAIDAAYAAGGGTVYL
PAGEYRVSAAGEPGDGCLMLKDGVYLAGAGMGETVIKL
IDGSDQKITGMVRSAYGEETSNFGMRDLTLDGNRDNTSG
KVDGWFNGYIPGGDGADRDTVIERVEVREMSGYGFDPH
EQTINLTIRDSVAHDNGLDGFVADYLVDSVFENNVAYAND
RHGFNVVTSTHDFVMTNNVAYGNGSSGLVVQRGLEDLAL
PSNILIDGGAYYDNAREGVLLKMTSDITLQNADIHGNGSSG
VRVYGAQDVQILDNQIHDNAQAAAVPEVLLQSFD D TAGA
SGTYYTTLNTRIEGNTISGSANSTYGIQERNDGTDYSSLID
NDIAGVQQPIQLYGPHSTVSGEPGATPQQPSTGSDGEPLV
GGDTDDQLQGGSGADRLDGGAGDDILDGGAGRDRLSGG
AGADTFVFSAREDSYRTDTAVFNDLILDFEASEDRIDLSAL
GFSGGLGDGYGGTLLLKTNAEGTRTYLKSFEADAEGRRFE
VALDGDHTGDLAANVVFAATGTTTELEVLGDSGTQAGA
IV

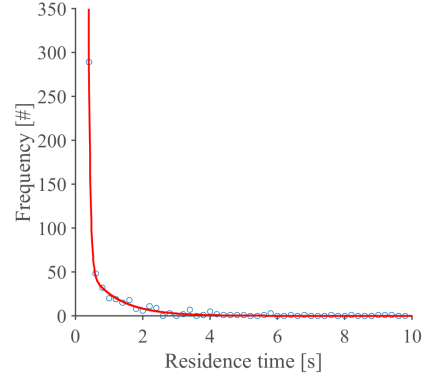
```

Figure A.3: Representation of the amino acid sequence of the entire Mannuronan C-5 Epimerase, including S-motif and linker residue [92].

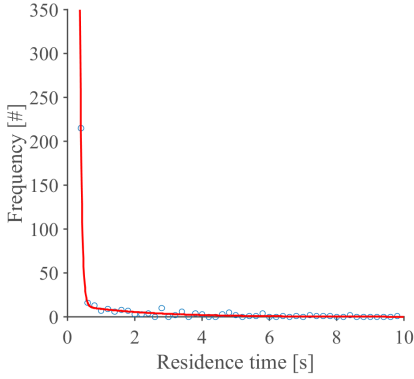
A.3 Results from fluctuation analysis



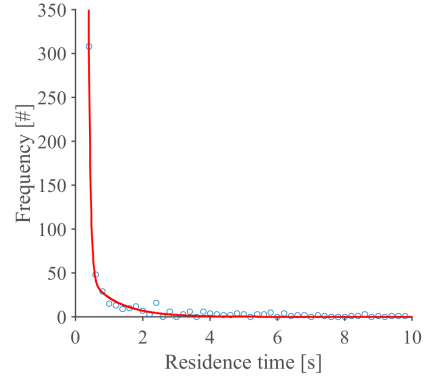
(a) Sample A, 100 000:1 EDAC:NP, functionalized with 0.9 mg/mL AlgE4.



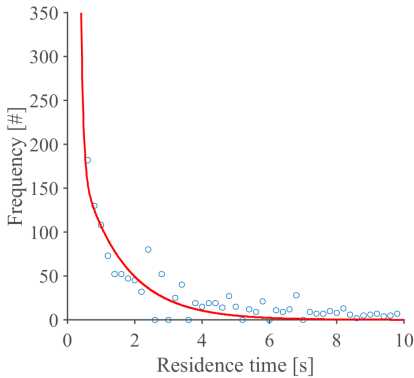
(b) Sample B, 1000:1 EDAC:NP, functionalized with 0.9 mg/mL AlgE4.



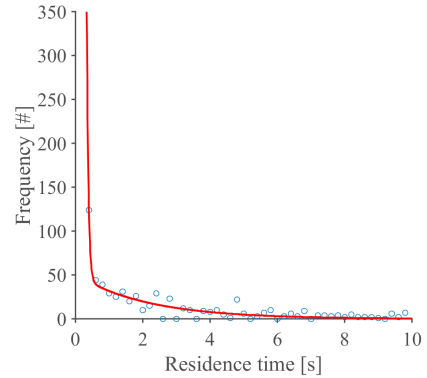
(c) Sample C, 100:1 EDAC:NP, functionalized with 0.9 mg/mL AlgE4.



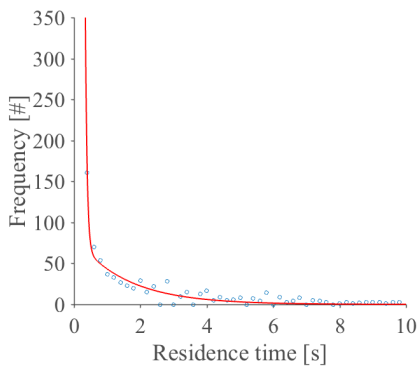
(d) Sample D, 10:1 EDAC:NP, functionalized with 0.9 mg/mL AlgE4.



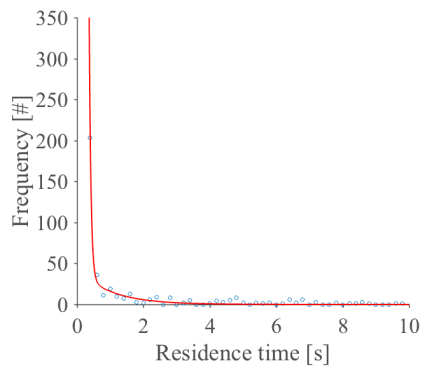
(e) Sample E, 100 000:1 EDAC:NP, no AlgE4.



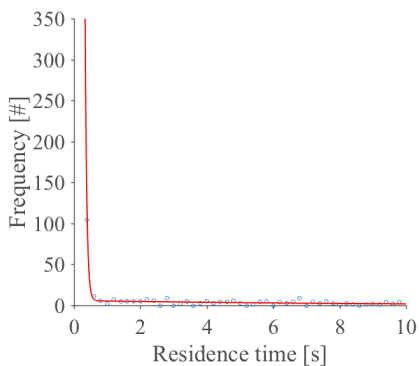
(f) Sample F, no EDAC, no AlgE4.



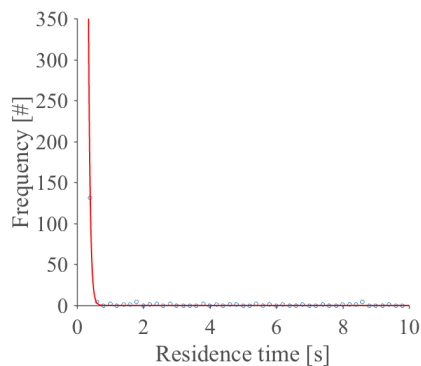
(a) Sample 2A, 100 000:1 EDAC:NP, functionalized with 0.9 mg/mL AlgE4.



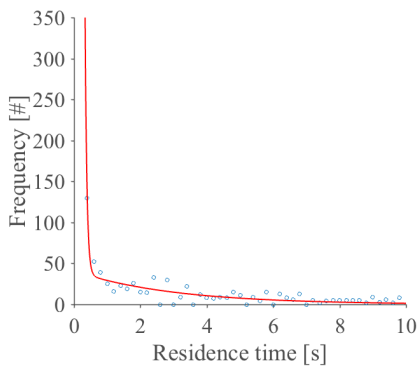
(b) Sample 2B, 1000:1 EDAC:NP, functionalized with 0.9 mg/mL AlgE4.



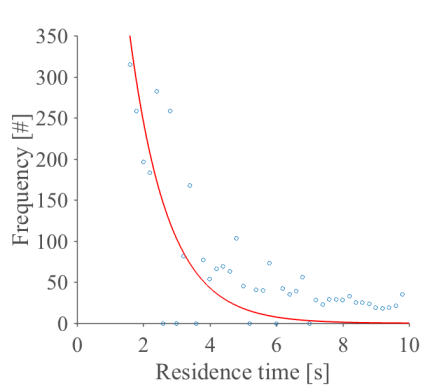
(c) Sample 2C, 100:1 EDAC:NP, functionalized with 0.9 mg/mL AlgE4.



(d) Sample 2D, 10:1 EDAC:NP, functionalized with 0.9 mg/mL AlgE4.



(e) Sample 2E, 100 000:1 EDAC:NP, no AlgE4.



(f) Sample 2F, no EDAC, no AlgE4.

Bibliography

- [1] Clark Leland C. and Lyons Champ. “ELECTRODE SYSTEMS FOR CONTINUOUS MONITORING IN CARDIOVASCULAR SURGERY”. *Annals of the New York Academy of Sciences* 102.1 (), pp. 29–45. DOI: [10.1111/j.1749-6632.1962.tb13623.x](https://doi.org/10.1111/j.1749-6632.1962.tb13623.x), eprint: <https://nyaspubs.onlinelibrary.wiley.com/doi/pdf/10.1111/j.1749-6632.1962.tb13623.x>, URL: <https://nyaspubs.onlinelibrary.wiley.com/doi/abs/10.1111/j.1749-6632.1962.tb13623.x>.
- [2] Harshini Mukundan et al. “Waveguide-Based Biosensors for Pathogen Detection”. *Sensors* 9.7 (2009), pp. 5783–5809. ISSN: 1424-8220. DOI: [10.3390/s90705783](https://doi.org/10.3390/s90705783), URL: <http://www.mdpi.com/1424-8220/9/7/5783>.
- [3] Dorothee Grieshaber et al. “Electrochemical Biosensors - Sensor Principles and Architectures”. *Sensors (Basel, Switzerland)* 8.3 (Mar. 2008), pp. 1400–1458. URL: <http://www.ncbi.nlm.nih.gov/pmc/articles/PMC3663003/>.
- [4] Carlos Bustamante. “In singulo Biochemistry: When Less Is More”. *Annual Review of Biochemistry* 77.1 (2008). PMID: 18518817, pp. 45–50. DOI: [10.1146/annurev.biochem.012108.120952](https://doi.org/10.1146/annurev.biochem.012108.120952), eprint: <https://doi.org/10.1146/annurev.biochem.012108.120952>, URL: <https://doi.org/10.1146/annurev.biochem.012108.120952>.
- [5] Nina Arnfinnsdottir. “Schematic illustration of a photonic biosensor”. Department of Physics, NTNU. Dec. 2018.
- [6] Anders Gunnarsson et al. “Single-Molecule Detection and Mismatch Discrimination of Unlabeled DNA Targets”. *Nano Letters* 8.1 (2008). PMID: 18088151, pp. 183–188. DOI: [10.1021/nl072401j](https://doi.org/10.1021/nl072401j), eprint: <https://doi.org/10.1021/nl072401j>, URL: <https://doi.org/10.1021/nl072401j>.
- [7] Corzo Javier. “Time, the forgotten dimension of ligand binding teaching”. *Biochemistry and Molecular Biology Education* 34.6 (), pp. 413–416. DOI: [10.1002/](https://doi.org/10.1002/)

- bmb . 2006 . 494034062678. eprint: <https://iubmb.onlinelibrary.wiley.com/doi/pdf/10.1002/bmb.2006.494034062678>. URL: <https://iubmb.onlinelibrary.wiley.com/doi/abs/10.1002/bmb.2006.494034062678>.
- [8] Thomas D Pollard. “A Guide to Simple and Informative Binding Assays”. *Molecular Biology of the Cell* 21.23 (Dec. 2010). Ed. by Douglas Kellogg, pp. 4061–4067. DOI: [10.1091/mbc.E10-08-0683](https://doi.org/10.1091/mbc.E10-08-0683). URL: <http://www.ncbi.nlm.nih.gov/pmc/articles/PMC2993736/>.
- [9] Albert C. Pan et al. “Molecular determinants of drug–receptor binding kinetics”. *Drug Discovery Today* 18.13 (2013), pp. 667–673. ISSN: 1359-6446. DOI: <https://doi.org/10.1016/j.drudis.2013.02.007>. URL: <http://www.sciencedirect.com/science/article/pii/S1359644613000627>.
- [10] Dynamic Biosensors Ulrich Rant. *Binding Theory Binding Theory: Equations for Affinity and Kinetics Analysis*. URL: https://www.dynamic-biosensors.com/wpcms/wp-content/uploads/2016/05/TechNote_101_Binding-Theory.pdf (visited on).
- [11] Jacob N. Israelachvili. *Intermolecular and Surface Forces*. 3rd ed. Elsevier, 2011.
- [12] Jan Theodoor Gerard Overbeek Evert Johannes Willem Verwey. *Theory of the Stability of Lyophobic Colloids*. Ed. by K. Van Nes. 1. Elsevier Publishing Corporation, 1948.
- [13] C. Berli D. Quemada. “Energy of interaction in colloids and its implications in rheological modeling.” *Advances in Colloid and Interface Science* 98.1 (2002), pp. 51–85.
- [14] Lindhoud S. et al. N. Lebovka C. Cramer. “Polyelectrolyte Complexes in the Dispersed and Solid State I”. Ed. by Martin Müller. 1. Springer, 2014, pp. 57–96.
- [15] Gregor Trefalt and Michal Borkovec. *Overview of DLVO Theory*. URL: www.colloid.ch/dlvo (visited on).
- [16] P. G. de Gennes. “Polymers at an interface; a simplified view”. *Advances in Colloid and Interface Science* 27.3 (1987), pp. 189–209. DOI: [https://doi.org/10.1016/0001-8686\(87\)85003-0](https://doi.org/10.1016/0001-8686(87)85003-0). URL: <http://www.sciencedirect.com/science/article/pii/0001868687850030>.
- [17] Roberto Piazza, Tommaso Bellini, and Vittorio Degiorgio. “Equilibrium sedimentation profiles of screened charged colloids: A test of the hard-sphere equation of state”. *Physical Review Letters* 71.25 (Dec. 1993), pp. 4267–4270. DOI: [10.1103/PhysRevLett.71.4267](https://doi.org/10.1103/PhysRevLett.71.4267). URL: <https://link.aps.org/doi/10.1103/PhysRevLett.71.4267>.

- [18] Cole-Parmer Scientific Experts. *Eppendorf 22 36 411-1 Microcentrifuge Tubes; capacity, 1.5 mL*. URL: <https://www.coleparmer.com/i/eppendorf-22-36-411-1-microcentrifuge-tubes-capacity-1-5-ml-500-pack/0255007>.
- [19] Jess Willcoxon. "Validity of Stokes' Law for Polystyrene Latex Spheres". *Biopolymers* 22 (1983), pp. 1023–1025.
- [20] Stefano Buzzaccaro et al. "Kinetics of sedimentation in colloidal suspensions". *Journal of Physics: Condensed Matter* 20.49 (2008), p. 494219. URL: <http://stacks.iop.org/0953-8984/20/i=49/a=494219>.
- [21] Hugh D Newman and Anand Yethiraj. "Clusters in sedimentation equilibrium for an experimental hard-sphere-plus-dipolar Brownian colloidal system". *Scientific Reports* 5 (2015), p. 13572. DOI: [10.1038/srep13572](https://doi.org/10.1038/srep13572) URL: <http://www.ncbi.nlm.nih.gov/pmc/articles/PMC4555105/>.
- [22] Ori Zvikelsky and Noam Weisbrod. "Impact of particle size on colloid transport in discrete fractures". *WATER RESOURCES RESEARCH* 42 (2006).
- [23] Alan Rawle. *Basic principles of particle size analysis*. Tech. rep. Enigma Business Park, Grovewood Road, Malvern, Worcestershire, WR14 1XZ, UK: Malvern Instruments Limited.
- [24] Roberto Piazza. "Settled and unsettled issues in particle settling". *Reports on Progress in Physics* 77.5 (2014).
- [25] Thermo Fisher Scientific. *Working With FluoSpheres Fluorescent Microspheres*. URL: <https://tools.thermofisher.com/content/sfs/manuals/mp05001.pdf>.
- [26] Michael J Sanderson et al. "Fluorescence Microscopy". *Cold Spring Harbor protocols* 2014.10 (Oct. 2014), pdb.top071795–pdb.top071795. DOI: [10.1101/pdb.top071795](https://doi.org/10.1101/pdb.top071795) URL: <http://www.ncbi.nlm.nih.gov/pmc/articles/PMC4711767/>.
- [27] Ghauharali and Brakenhoff. "Fluorescence photobleaching-based image standardization for fluorescence microscopy". *Journal of Microscopy* 198.2 (), pp. 88–100. DOI: [10.1046/j.1365-2818.2000.00683.x](https://doi.org/10.1046/j.1365-2818.2000.00683.x) eprint: <https://onlinelibrary.wiley.com/doi/pdf/10.1046/j.1365-2818.2000.00683.x> URL: <https://onlinelibrary.wiley.com/doi/abs/10.1046/j.1365-2818.2000.00683.x>.
- [28] Alexa L Mattheyses, Sanford M Simon, and Joshua Z Rappoport. "Imaging with total internal reflection fluorescence microscopy for the cell biologist". *Journal of Cell Science* 123.21 (Nov. 2010), pp. 3621–3628. DOI: [10.1242/jcs.056218](https://doi.org/10.1242/jcs.056218) URL: <http://www.ncbi.nlm.nih.gov/pmc/articles/PMC2964103/>.
- [29] Park Systems. *Phase Imaging of Sample Elasticity*. URL: <https://www.parksystems.com/index.php/park-spm-modes/91-standard-imaging-mode/221-phase-imaging-phase-detection-microscopy-pdm> (visited on).

- [30] W.D Brandon D.; Kaplan. *Microstructural Characterization of Materials*. Ed. by D. Brandon. 2. Wiley, 2008.
- [31] Ivo Sbalzarini and Petros Koumoutsakos. "Feature point tracking and trajectory analysis for video imaging in cell biology". 151 (Sept. 2005), pp. 182–95.
- [32] N. Chenouard, I. Bloch, and J. C. Olivo-Marin. "Multiple Hypothesis Tracking for Cluttered Biological Image Sequences". *IEEE Transactions on Pattern Analysis and Machine Intelligence* 35.11 (2013), pp. 2736–3750. DOI: [10.1109/TPAMI.2013.97](https://doi.org/10.1109/TPAMI.2013.97).
- [33] Nicolas Chenouard et al. "Objective comparison of particle tracking methods". *Nature Methods* 11 (Jan. 2014), 281 EP -. URL: <http://dx.doi.org/10.1038/nmeth.2808>.
- [34] Maria-José Bañuls, Rosa Puchades, and Ángel Maquieira. "Chemical surface modifications for the development of silicon-based label-free integrated optical (IO) biosensors: A review". *Analytica Chimica Acta* 777 (2013), pp. 1–16. ISSN: 0003-2670. DOI: <https://doi.org/10.1016/j.aca.2013.01.025>, URL: <http://www.sciencedirect.com/science/article/pii/S0003267013001736>.
- [35] Silje Uhlen Maurseth. "Functionalization of a Photonic Biosensor". MA thesis. Norwegian University of Science and Technology, 2016.
- [36] Y. Han et al. "Surface activation of thin silicon oxides by wet cleaning and silanization". *Thin Solid Films* 510.1 (2006), pp. 175–180. DOI: <https://doi.org/10.1016/j.tsf.2005.11.048>, URL: <http://www.sciencedirect.com/science/article/pii/S0040609005022571>.
- [37] Thermo Fisher Scientific. *Carbodiimide Crosslinker Chemistry*. URL: <https://www.thermofisher.com/no/en/home/life-science/protein-biology/protein-biology-learning-center/protein-biology-resource-library/pierce-protein-methods/carbodiimide-crosslinker-chemistry.html>.
- [38] Joydeep Lahiri et al. "A Strategy for the Generation of Surfaces Presenting Ligands for Studies of Binding Based on an Active Ester as a Common Reactive Intermediate: A Surface Plasmon Resonance Study". *Analytical Chemistry* 71.4 (Feb. 1999), pp. 777–790. DOI: [10.1021/ac980959t](https://doi.org/10.1021/ac980959t), URL: <https://doi.org/10.1021/ac980959t>.
- [39] Nick R Glass et al. "Organosilane deposition for microfluidic applications". *Biomicrofluidics* 5.3 (Sept. 2011), pp. 036501–036501-7. DOI: [10.1063/1.3625605](https://doi.org/10.1063/1.3625605), URL: <http://www.ncbi.nlm.nih.gov/pmc/articles/PMC3364836/>.
- [40] Thermo Fisher Scientific. *Working With FluoSpheres FLuorescent Microspheres*. URL: <https://tools.thermofisher.com/content/sfs/manuals/mp05001.pdf>.

- [41] Tonje Marita Bjerkan. “Structure - Function Analyses of Mannuronan C-5-epimerases. - A Family of Modular Type Enzymes with an Applied Potential”. PhD thesis. NTNU, 2004.
- [42] Henriëtte J. Rozeboom et al. “Structural and Mutational Characterization of the Catalytic A-module of the Mannuronan C-5-epimerase AlgE4 from *Azotobacter vinelandii*”. *Journal of Biological Chemistry* 283.35 (Aug. 2008), pp. 23819–23828. DOI: [10.1074/jbc.M804119200](https://doi.org/10.1074/jbc.M804119200).
- [43] Britt Iren Glærum Svanem et al. “Cloning and Expression of Three New *Azotobacter vinelandii* Genes Closely Related to a Previously Described Gene Family Encoding Mannuronan C-5-Epimerases”. *Journal of Bacteriology* 181.1 (Jan. 1999), pp. 68–77. URL: <http://www.ncbi.nlm.nih.gov/pmc/articles/PMC103533/>.
- [44] Michael Sinnott. *Carbohydrate Chemistry and Biochemistry: Structure and Mechanism*. Ed. by Michael Sinnott. 2. Royal Society of Chemistry, 2013.
- [45] Lukasz P. Kozlowski. “IPC –Isoelectric Point Calculator”. *Biology Direct* 11.1 (2016), p. 55. DOI: [10.1186/s13062-016-0159-9](https://doi.org/10.1186/s13062-016-0159-9). URL: <https://doi.org/10.1186/s13062-016-0159-9>.
- [46] Finn L. Aachmann et al. “NMR Structure of the R-module: A PARALLEL -ROLL SUBUNIT FROM AN AZOTOBACTER VINELANDII MANNURONAN C-5 EPIMERASE”. *Journal of Biological Chemistry* 281.11 (Mar. 2006), pp. 7350–7356. DOI: [10.1074/jbc.M510069200](https://doi.org/10.1074/jbc.M510069200).
- [47] Marit Sletmoen, Gudmund Skjåk-Bræk, and Bjørn T. Stokke. “Mapping enzymatic functionalities of mannuronan C-5 epimerases and their modular units by dynamic force spectroscopy”. *Carbohydrate Research* 340.18 (2005), pp. 2782–2795. ISSN: 0008-6215. DOI: <https://doi.org/10.1016/j.carres.2005.09.020>. URL: <http://www.sciencedirect.com/science/article/pii/S0008621505004611>.
- [48] Armend Gazmeno Håti et al. “Energy Landscape of Alginate-Epimerase Interactions Assessed by Optical Tweezers and Atomic Force Microscopy”. *PLOS ONE* 10.10 (2015), pp. 1–19. DOI: [10.1371/journal.pone.0141237](https://doi.org/10.1371/journal.pone.0141237). URL: <https://doi.org/10.1371/journal.pone.0141237>.
- [49] Martin Gimmetstad et al. “The *Pseudomonas fluorescens* AlgG Protein, but Not Its Mannuronan C-5-Epimerase Activity, Is Needed for Alginate Polymer Formation”. *Journal of Bacteriology* 185.12 (June 2003), pp. 3515–3523. DOI: [10.1128/JB.185.12.3515-3523.2003](https://doi.org/10.1128/JB.185.12.3515-3523.2003). URL: <http://www.ncbi.nlm.nih.gov/pmc/articles/PMC156231/>.

- [50] H K Høidal et al. “The Recombinant *Azotobacter vinelandii* Mannuronan C-5-Epimerase AlgE4 Epimerizes Alginate by a Nonrandom Attack Mechanism”. 274 (May 1999), pp. 12316–22.
- [51] Jose Luis Lepe-Zuniga, J. S. Zigler, and Igal Gery. “Toxicity of light-exposed Hepes media”. *Journal of Immunological Methods* 103.1 (1987), p. 145. DOI: [https://doi.org/10.1016/0022-1759\(87\)90253-5](https://doi.org/10.1016/0022-1759(87)90253-5). URL: <http://www.sciencedirect.com/science/article/pii/0022175987902535>.
- [52] Sebastian Rhode. *Calculate TIRF*. URL: <https://imagej.nih.gov/ij/plugins/tirf/index.html>.
- [53] Chuanjun Liu, Elmar Bonaccorso, and Hans-Jurgen Butt. “Evaporation of sessile water/ethanol drops in a controlled environment”. *Phys. Chem. Chem. Phys.* 10 (47 2008), pp. 7150–7157. DOI: [10.1039/B808258H](https://doi.org/10.1039/B808258H). URL: <http://dx.doi.org/10.1039/B808258H>.
- [54] University of Delaware Furst Research Group. *Particle Tracking Handout*. URL: http://lem.che.udel.edu/sandbox/groups/furstgroupwiki/wiki/7672a/attachments/25e13/Handout_particle_tracking.pdf
- [55] Primate Labs. *Geekbench browser*. URL: <https://browser.geekbench.com/processors/571>.
- [56] Thermo Fisher Scientific. *Latex Bead Technical Overview*. URL: <https://www.thermofisher.com/us/en/home/life-science/cell-analysis/qdots-microspheres-nanospheres/idc-surfactant-free-latex-beads/latex-bead-technical-overview.html> (visited on).
- [57] Paweł Śledź et al. “An experimental charge density of HEPES”. *Acta Crystallographica Section B* 66.4 (Aug. 2010), pp. 482–492. DOI: [10.1107/S0108768110023025](https://doi.org/10.1107/S0108768110023025). URL: <https://doi.org/10.1107/S0108768110023025>.
- [58] Earle Stellwagen, Jason D. Prantner, and Nancy C. Stellwagen. “Do zwitterions contribute to the ionic strength of a solution?” *Analytical Biochemistry* 373.2 (2008), pp. 407–409. DOI: <https://doi.org/10.1016/j.ab.2007.10.038>. URL: <http://www.sciencedirect.com/science/article/pii/S0003269707007099>.
- [59] “CRC Handbook of Chemistry and Physics”. Ed. by Charles D. Hodgman. 90. CRC Press/Taylor Francis, 2009. Chap. 3.
- [60] Christy Charlton et al. “TIRF microscopy as a screening method for non-specific binding on surfaces”. *Journal of colloid and interface science* 354 (Oct. 2010), pp. 405–9. DOI: [10.1016/j.jcis.2010.10.029](https://doi.org/10.1016/j.jcis.2010.10.029).

- [61] Amy Tekrony and David Cramb. *Determination of the Mobility of Amine- and Carboxy-Terminated Fluospheres and Quantum Dots by Capillary Electrophoresis*. Vol. 94. Jan. 2016. DOI: [10.1139/cjc-2015-0349](https://doi.org/10.1139/cjc-2015-0349).
- [62] Vladimir Gubala et al. "Simple approach to study biomolecule adsorption in polymeric microfluidic channels". *Analytica Chimica Acta* 760 (2013), pp. 75–82. DOI: <https://doi.org/10.1016/j.aca.2012.11.030>. URL: <http://www.sciencedirect.com/science/article/pii/S0003267012017060>.
- [63] Luca Medda, Maura Monduzzi, and Andrea Salis. "The molecular motion of bovine serum albumin under physiological conditions is ion specific". *Chemical Communications* 51.30 (2015), pp. 6663–6666. DOI: [10.1039/C5CC01538C](https://doi.org/10.1039/C5CC01538C). URL: <http://dx.doi.org/10.1039/C5CC01538C>.
- [64] Technical Service. *ALBUMIN FROM BOVINE SERUM Product Information*. 3050 Spruce Stree, Saint Luis, MO 63103 USA: Sigma Aldrich. URL: https://www.sigmaaldrich.com/content/dam/sigma-aldrich/docs/Sigma/Product_Information_Sheet/b2518pis.pdf.
- [65] Guillaume Suárez et al. "Biomolecule Patterning on Analytical Devices: A Microfabrication-Compatible Approach". *Langmuir* 26.8 (Apr. 2010), pp. 6071–6077. DOI: [10.1021/la904527s](https://doi.org/10.1021/la904527s). URL: <https://doi.org/10.1021/la904527s>.
- [66] Sven H. Behrens and David G. Grier. "The Charge of Glass and Silica Surfaces". *The Journal of Chemical Physics* 115 (2001). Department of Physics, James Franck Institute, and Institute for Biophysical Dynamics, The University of Chicago, Chicago, IL 60637, pp. 6716–6721.
- [67] Vladimir Gubalaa and Jonathan Siegris. "Simple approach to study biomolecule adsorption in polymeric microfluidic channels". *Analytica Chimica Acta* 760 (2013), pp. 75–82.
- [68] Caner Nazli et al. *RGDS-functionalized polyethylene glycol hydrogel-coated magnetic iron oxide nanoparticles enhance specific intracellular uptake by HeLa cells*. Vol. 7. Apr. 2012, pp. 1903–20. DOI: [10.2147/IJN.S29442](https://doi.org/10.2147/IJN.S29442).
- [69] Anisha A. D'souza and Ranjita Shegokar. "Polyethylene glycol (PEG): a versatile polymer for pharmaceutical applications". *Expert Opinion on Drug Delivery* 13.9 (Sept. 2016), pp. 1257–1275. DOI: [10.1080/17425247.2016.1182485](https://doi.org/10.1080/17425247.2016.1182485). URL: <https://doi.org/10.1080/17425247.2016.1182485>.
- [70] W. Slingenbergh E. Ploetz B. Visser. "Selective functionalization of patterned glass surfaces". *Journal of Materials Chemistry* 2.<http://pubs.rsc.org/en/Content/ArticleHtml/2014> (2014), pp. 2606–2615.

- [71] Stanley D Chandradoss et al. "Surface Passivation for Single-molecule Protein Studies". *Journal of Visualized Experiments : JoVE* 86 (2014), p. 50549. DOI: [10.3791/50549](https://doi.org/10.3791/50549). URL: <http://www.ncbi.nlm.nih.gov/pmc/articles/PMC4179479/>.
- [72] Kjetil Formo Therese Anders Berit L. Strand. "Alginates as biomaterials in tissue engineering". *Carbohydrate Chemistry* 37 (2012), pp. 227–258.
- [73] J. S. Zigler et al. "Analysis of the cytotoxic effects of light-exposed hepes-containing culture medium". *In Vitro Cellular & Developmental Biology* 21.5 (1985), pp. 282–287. DOI: [10.1007/BF02620943](https://doi.org/10.1007/BF02620943). URL: <https://doi.org/10.1007/BF02620943>.
- [74] Kristin E. Haugstad et al. "Enhanced Self-Association of Mucins Possessing the T and Tn Carbohydrate Cancer Antigens at the Single-Molecule Level". *Biomacromolecules* 13.5 (May 2012), pp. 1400–1409. DOI: [10.1021/bm300135h](https://doi.org/10.1021/bm300135h). URL: <https://doi.org/10.1021/bm300135h>.
- [75] Naoki Nakajima and Yoshito Ikada. "Mechanism of Amide Formation by Carbodiimide for Bioconjugation in Aqueous Media". *Bioconjugate Chemistry* 6.1 (Jan. 1995), pp. 123–130. DOI: [10.1021/bc00031a015](https://doi.org/10.1021/bc00031a015). URL: <https://doi.org/10.1021/bc00031a015>.
- [76] S. Sam et al. "Semiquantitative Study of the EDC/NHS Activation of Acid Terminal Groups at Modified Porous Silicon Surfaces". *Langmuir* 26.2 (Jan. 2010), pp. 809–814. DOI: [10.1021/la902220a](https://doi.org/10.1021/la902220a). URL: <https://doi.org/10.1021/la902220a>.
- [77] Hongyan Shen, Ali M. Jawaid, and Preston T. Snee. "Poly(ethylene glycol) Carbodiimide Coupling Reagents for the Biological and Chemical Functionalization of Water-Soluble Nanoparticles". *ACS Nano* 3.4 (Apr. 2009), pp. 915–923. DOI: [10.1021/nn800870r](https://doi.org/10.1021/nn800870r). URL: <https://doi.org/10.1021/nn800870r>.
- [78] Sperling R. A. et al. "Electrophoretic Separation of Nanoparticles with a Discrete Number of Functional Groups". *Advanced Functional Materials* 16.7 (2018/06/10 2006), pp. 943–948. DOI: [10.1002/adfm.200500589](https://doi.org/10.1002/adfm.200500589). URL: <https://doi.org/10.1002/adfm.200500589>.
- [79] Andrew Collins. *Nanotechnology Cookbook: Practical, Reliable and Jargon-free Experimental Procedures*. 1st ed. Elsevier, 2012, pp. 127–128.
- [80] Maxime A. Gilles, Antoine Q. Hudson, and C. L. Borders. "Stability of water-soluble carbodiimides in aqueous solution". *Analytical Biochemistry* 184.2 (1990), pp. 244–248. DOI: [https://doi.org/10.1016/0003-2697\(90\)90675-Y](https://doi.org/10.1016/0003-2697(90)90675-Y). URL: <http://www.sciencedirect.com/science/article/pii/000326979090675Y>.

- [81] João Conde et al. *Revisiting 30 years of Biofunctionalization and Surface Chemistry of Inorganic Nanoparticles for Nanomedicine*. Vol. 2. June 2014. DOI: [10.3389/fchem.2014.00048](https://doi.org/10.3389/fchem.2014.00048).
- [82] Vanesa Sanz et al. "Effect of PEG biofunctional spacers and TAT peptide on dsRNA loading on gold nanoparticles". *Journal of Nanoparticle Research* 14.6 (2012), p. 917. DOI: [10.1007/s11051-012-0917-2](https://doi.org/10.1007/s11051-012-0917-2). URL: <https://doi.org/10.1007/s11051-012-0917-2>.
- [83] Atilio de Oliveira Cardoso and Fernando Galembeck. "Polymer Latex Stability Modification by Exposure to Hydrophobic Solvents". *Journal of Colloid and Interface Science* 204.1 (1998), pp. 16–23. DOI: <https://doi.org/10.1006/jcis.1998.5451>. URL: <http://www.sciencedirect.com/science/article/pii/S0021979798954510>.
- [84] B. R. Midmore and R. J. Hunter. "The effect of electrolyte concentration and cation type on the ζ -potential of polystyrene latices". *Journal of Colloid and Interface Science* 122.2 (1988), pp. 521–529. DOI: [https://doi.org/10.1016/0021-9797\(88\)90387-6](https://doi.org/10.1016/0021-9797(88)90387-6). URL: <http://www.sciencedirect.com/science/article/pii/0021979788903876>.
- [85] Dayong Jin et al. "Nanoparticles for super-resolution microscopy and single-molecule tracking". *Nature Methods* 15.6 (2018), pp. 415–423. DOI: [10.1038/s41592-018-0012-4](https://doi.org/10.1038/s41592-018-0012-4). URL: <https://doi.org/10.1038/s41592-018-0012-4>.
- [86] A. M. Moulin et al. "Measuring Surface-Induced Conformational Changes in Proteins". *Langmuir* 15.26 (Dec. 1999), pp. 8776–8779. DOI: [10.1021/la990416u](https://doi.org/10.1021/la990416u). URL: <https://doi.org/10.1021/la990416u>.
- [87] Wolfgang J. Parak et al. "Conformation of Oligonucleotides Attached to Gold Nanocrystals Probed by Gel Electrophoresis". *Nano Letters* 3.1 (Jan. 2003), pp. 33–36. DOI: [10.1021/nl025888z](https://doi.org/10.1021/nl025888z). URL: <https://doi.org/10.1021/nl025888z>.
- [88] Dorota Bartczak and Antonios G. Kanaras. "Preparation of Peptide-Functionalized Gold Nanoparticles Using One Pot EDC/Sulfo-NHS Coupling". *Langmuir* 27.16 (Aug. 2011), pp. 10119–10123. DOI: [10.1021/la2022177](https://doi.org/10.1021/la2022177). URL: <https://doi.org/10.1021/la2022177>.
- [89] Thermo Fisher Scientific. *Avidin-Biotin Interaction*. URL: <https://www.thermofisher.com/no/en/home/life-science/protein-biology/protein-biology-learning-center/protein-biology-resource-library/pierce-protein-methods/avidin-biotin-interaction.html>.

-
- [90] João Conde et al. *Revisiting 30 years of Biofunctionalization and Surface Chemistry of Inorganic Nanoparticles for Nanomedicine*. Vol. 2. June 2014. DOI: [10.3389/fchem.2014.00048](https://doi.org/10.3389/fchem.2014.00048).
- [91] Research Institute of Physical-Chemical Medicine. *Centrifugation Parameters Calculator*. URL: <http://vesicles.niifhm.ru/index.php?do=1>.
- [92] European Molecular Biology Laboratory. *Protein Data Bank in Europe*. URL: <https://www.ebi.ac.uk/pdbe/>.